Research Square

Preprints are preliminary reports that have not undergone peer review.
They should not be considered conclusive, used to inform clinical practice,
or referenced by the media as validated information.

Metabolic rewiring promotes metastasis while enhancing NK cell recognition

Sara Zemiti

sara.zemiti@inserm.fr

Inserm U1183

Susana Prieto

CNRS UMR 5535

Steffy Escayg

Inserm U1183

Benjamin Hay

Inserm U1183

Amel Bouzid

Inserm U1183

Catherine Alexia

University of Montpellier

Carine Jacquard

Inserm U1183

Noemie Dudzinska

Inserm U1183

Ananya Sen

Inserm U1183

Jose Prudenciano

Inserm U1183

Daouda Abba Moussa

Inserm U1183

Mauricio Campos Mora

Inserm U1183

Sabine Gerbal-Chaloin

Institut de Recherche en Biothérapie

Michael Constantinides

Inserm U1183

Alberto Anel

Marion De Toledo

CNRS UMR 5535

Guillaume Bossis
CNRS https://orcid.org/0000-0002-3349-8250
Ana-Bella Aznar
CNRS UMR 5535
Daniel Fisher
CNRS https://orcid.org/0000-0002-0822-3482
farida djouad
INSERM U1183
Yoan Arribat
Inserm U1183
Jean-François Rossi
Institut du Cancer Avignon-Provence Sainte Catherine
Martin Villalba
INSERM U1183 - Institute for Regenerative Medicine & Biotherapy https://orcid.org/0000-0002-4385-4888
Delphine Gitenay
University of Montpellier

Article

Keywords:

Posted Date: August 24th, 2026

DOI: https://doi.org/10.21203/rs.3.rs-9565218/v1

License: This work is licensed under a Creative Commons Attribution 4.0 International License.
Read Full License

Additional Declarations: (Not answered)

Abstract

To colonize new environments, cancer cells undergo epithelial-to-mesenchymal transition (EMT), enabling detachment and migration, but this phenomenon remains largely controlled by Natural Killer (NK) cells. During EMT, cancer cells shift their metabolism toward fatty acid oxidation (FAO), partly replacing glycolysis to meet the energy demands for migration and invasion. This may impact NK cell-mediated surveillance through an unclear mechanism. Here, we demonstrate that forcing cancer cells to perform FAO by inhibiting pyruvate dehydrogenase kinase 1 with dichloroacetate (DCA) decreases intracellular palmitic and stearic acids, reflecting their utilization as FAO substrates, whereas the rise in neutral lipids reflects compensatory lipid-droplet formation, a hallmark of FAO-driven states linked to EMT. Moreover, DCA activates extracellular signal-regulated kinase-5 (ERK5), triggering EMT and tumor cell migration and invasion. Concomitantly, FAO induces ligands mediating NK cell recognition. NK cells better infiltrated DCA-treated 3D tumor spheroids, where they exerted cytotoxic effects. DCA-treated cells showed increased migration in a zebrafish model, whereas metastasis from mammary cancer cells grafted into immune-deficient mice was enhanced by DCA. Cells undergoing DCA-induced migratory reprogramming exhibit increased susceptibility to NK-cell-mediated control, which limit their invasive potential. Hence, FAO promotes both metastasis and NK-mediated tumor surveillance, highlighting the Achilles' heel of metastatic cells and therapeutic opportunities.

Teaser

Metastasis recognition and killing by immune cells, such as NK cells, requires a metabolic shift that relies on lipid metabolism.

Introduction

Cancer cells undergo profound metabolic reprogramming, relying heavily on glycolysis to meet the bioenergetic and biosynthetic requirements of rapid growth; aerobic glycolysis is therefore considered a hallmark of cancer(1). Beyond glycolysis, additional metabolic alterations have been described, including changes in amino acid and fatty acid (FA) metabolism, which can result in concomitant increases in both mitochondrial respiration and glycolysis(2). Cancer cells also adapt their metabolism in response to microenvironmental changes, particularly during metastatic colonization, a highly inefficient process in which disseminated tumor cells must overcome substantial physiological barriers to form secondary lesions(3). Once established, metastatic tumors often exhibit limited responses to existing therapies. Throughout dissemination, tumor cells encounter nutrient fluctuations and metabolic stress, to which they respond by increasing FA uptake and energy production through FA β-oxidation (FAO) (4). FAO-driven lipid oxidation thereby supports mitochondrial respiration and has been implicated in tumor progression, invasion, and metastasis. Notably, the FA transporter CD36 functions as a marker of metastasis-initiating cells (5, 6) and contributes to epithelial–mesenchymal transition (EMT) and tumor cell migration (6, 7).

Acyl-CoA synthetases (ACSLs) catalyze the activation of long-chain FAs into acyl-CoA, a crucial step for phospholipid and triglyceride synthesis, lipidation of proteins, and FAO (8). ACSL enzymes have been linked to EMT (9, 10), a key process enabling cancer cells to detach from the primary tumor and initiate metastatic dissemination. During their transit within the host, metastatic cells are exposed to immune surveillance, particularly from cytotoxic lymphocytes patrolling the blood and lymphatic systems. Natural killer (NK) cells play a central role in metastasis-specific immunosurveillance (11), and NK cell abundance and activity correlate with the number of circulating tumor cells and metastatic burden across several cancers (12). However, the mechanisms that govern NK-mediated recognition and elimination of metastatic cells remain incompletely understood. In a TGF-β-induced EMT model, Chockley et al. demonstrated that E-cadherin (E-Cad) is detected by the inhibitory NK receptor KLRG1 (11), whereas cell adhesion molecule 1 (CADM1) is recognized by the activating NK receptor CRTAM (11). Consequently, EMT-associated decreases in E-Cad and increases in CADM1 enhance NK recognition of metastatic cells, although loss of inhibitory E-Cad/KLRG1 signaling alone is insufficient to fully restore NK cytotoxicity (11). NK cells also suppress dormant tumor cells that can later regenerate malignancies long after the primary tumor has been removed (13).

NK cell recognition depends on the repertoire of surface ligands expressed on target cells. Several ligands for NK-activating receptors such as Poliovirus Receptor (PVR/CD155), ULBP2, ULBP4, and MICA/B are upregulated during EMT (14). Engagement of these ligands by the activating receptor NKG2D triggers NK-mediated cytotoxicity (15). In contrast, expression of major histocompatibility complex-I (MHC-I), which binds inhibitory NK receptors (11, 16), is reduced during EMT (17), and consequently, MHC-I is reported to be downregulated in metastatic cells (18–20). Thus, EMT drives multiple changes that favor NK-mediated immune surveillance, potentially contributing to the overall inefficiency of metastatic colonization (12, 21).

Metabolic regulation strongly influences tumor immunogenicity by shaping the balance between activating and inhibitory ligands at the cell surface (22). Enforced OXPHOS increases MHC-I expression in leukemic cells (22–25). Metformin, which reduces glycolytic flux, upregulates ICAM-1 and enhances NK-mediated killing (26–28). Likewise, dichloroacetate (DCA), an inhibitor of pyruvate dehydrogenase kinase-1 (PDK1) that activates pyruvate dehydrogenase and promotes pyruvate entry into the Krebs cycle (29, 30), sensitizes leukemic cells to NK-mediated cytotoxicity (26). In hematological malignancies, DCA induces genes involved in lipid metabolism including LDLR, CD36, and ACADVL through ERK5 signaling (31, 32). ERK5 itself contributes to immune recognition (18, 23, 24) and regulates multiple cancer hallmarks (33), such as increased motility (33, 34) and EMT (33, 35). ERK5 therefore emerges as a compelling candidate linking metabolic rewiring, EMT, and immune surveillance (36).

Together, these observations support the hypothesis that increased lipid catabolism in cancer cells may promote EMT and early metastatic events while simultaneously inducing stress signals that activate NK cells. Such metabolic stress could thus enhance tumor cell immunogenicity and facilitate NK-mediated recognition and elimination. The work presented here supports this hypothesis. We artificially enhanced lipid catabolism by treating cancer cells with DCA. We characterized that this metabolic shift induces a

migratory phenotype both *in vitro* and *in vivo*, using two mouse models and a zebrafish model. Furthermore, metabolic stress promotes recognition and elimination by NK cells.

Results

DCA promotes lipid metabolic remodeling and increases respiration

To develop a cell model with increased FAO, HCT116 cells were treated for 48h with 5mM DCA alone or in combination with 3μM of the FA oleic acid (OA). DCA increased neutral lipid content, as shown by confocal microscopy (Fig. 1A) and flow cytometry (Fig. 1B), even more in the presence of OA. However, we noticed that DCA treatment had a tendency to increase cells size, in agreement with the cytostatic effect of DCA (26, 35, 37). To assess this change we quantified droplet accumulation per cell area and found no statistical differences (Supplemental Fig. 1). As in leukemic cells (31, 38), DCA increased *ACADVL* and *CD36* mRNA in HCT116 cells (Figs. 1C and D). Transfection with siRNA against *ERK5* (siERK5) partially reversed the effects of DCA on *ACADVL* and totally on *CD36* (Fig. 1C and D). DCA also increased CD36 expression at the plasma membrane (Fig. 1E). Adding OA or DCA to the cell culture medium was sufficient to increase the oxygen consumption (Fig. 1F). To further study DCA effect on lipid metabolism, we performed a metabolomic analysis in DCA-treated HCT116 cells. DCA significant decreased saturated long-chain fatty acids levels (Figs. 1G-H), particularly L-C16:0 (palmitic acid) and L-C18:0 (stearic acid). This suggests a metabolic shift from lipid synthesis toward enhanced β-oxidation, consistent with the known role of DCA in promoting oxidative metabolism through activation of the pyruvate dehydrogenase complex (39, 40) and with our results showing an increase of *ACADVL* mRNA relative expression (Fig. 1D and (4, 31).

DCA-induced lipid metabolism causes expression of EMT-related genes and a migratory phenotype

As DCA induced lipid metabolism, we hypothesized that it could favor a metastatic phenotype. In fact, DCA increased the mRNA levels of several critical genes to promote EMT, i.e. *ZEB1*, *SNAIL*, and *TWIST* (Fig. 2A). siERK5 partially reversed the effects of DCA on *ZEB1* and *SNAIL* and totally on *TWIST* (Fig. 2A). We confirmed the induction of SNAIL at the protein level, whereas the ERK5 inhibitor XMD8-92 reversed DCA effects (Fig. 2B). Hence, ERK5 mediates DCA effects on EMT. Consistent with these findings, flow cytometric analysis confirmed that DCA promoted a partial EMT phenotype in HCT116 cells, as evidenced by increased vimentin expression and a trend toward increased N-cadherin expression. Pharmacological inhibition of fatty acid oxidation with etomoxir partially reversed these changes, indicating that FAO contributes to DCA-induced EMT (Supplemental Fig. 2A).

The ERK5 pathway is involved in EMT and cell migration (34, 35). To investigate the effects of DCA on cell migration, we performed transwell assays. DCA increased HCT116 migration and co-addition of OA

did not increase DCA effects (Fig. 2C-D); although OA *per se* was able to induce migration. This could indicate that both compounds propel a similar mechanism. XMD8-92 completely blocked cell migration. In wound healing experiments, another model of metastatic potential, DCA induced wound closure similarly to TGF-β (Fig. 2E-F), a factor that induces EMT at least partially by promoting FA metabolism(37). XMD8-92 significantly inhibited wound healing (Fig. 2E-F) and reversed the effects of DCA. TGF-β induced the expression of *CD36, ACADVL* and *ERK5* along with EMT-related genes such as *SNAIL, ZEB1* and *TWIST* (Fig. 2H), but to a lesser extent than DCA (Fig. 2G-H). Finally, both TGF-β and DCA increased the expression of stress ligand genes (Fig. 2I), suggesting that changes in lipid metabolism may be implicated in multiple physiological processes (see below).

DCA favors cell motility and invasion in 3D cultures

To further assess the impact of DCA on HCT116 cell migration, we generated 3D tumor spheroids in ultra-low attachment (ULA) plates. DCA significantly reduced the spheroid area after seven days of treatment (Fig. 3A-B), showing that DCA also had cytostatic activity in 3D tumor cell cultures, as in 2D (37, 41) (41–43). Notably, DCA significantly increased the number of detached cells around the spheroids (Fig. 3A, C). We removed and pooled the spheroids, and separately pooled the remaining medium containing detached cells for each condition (Fig. 3D-E). DCA increased the expression of the same metabolic (CD36 and ACADVL) and EMT (ERK5, SNAIL and ZEB1) genes in 2D and 3D cultures. An increase was found in both the cells that stayed in the spheroid (Fig. 3D) and the cells that detached (Fig. 3E), with the exception of ACADVL, which did not change in detached cells and MHC-I that increased in attached cells, but decreased in detached cells. We also found that DCA increased the expression of the activating ligand for NK cell *ULBP4* and *PVR* in HCT116 cells grown in spheroids (Fig. 3D-E).

Next, we analyzed the invasive capacity of the spheroids treated with DCA. HCT116 cells were cultivated in ULA 96-well plates and after spheroid formation, they were transferred onto a 7% Geltrex matrix and treated with 10mM DCA each day (Fig. 3F-J). Without treatment and after 13 days, the control spheroid reached an average $2.48x10^6$ μm^2 whereas DCA-treated spheres only $3.8x10^5$ μm^2 (Fig. 3F, I). Thus, DCA limited spheroid size. Video capture shows the effects of DCA throughout the 16 days (Fig. 3G). In contrast, DCA favored cell migration and invasion of the surrounding environment and these invasive cells changed their phenotype (Fig. 3F-H). With DCA, the cells detached from each other and from the spheroid. To overcome the inherent problem of the variable spheroid sizes, we quantified the area that was occupied by cells outside the spheroid core, and called this “invasion area” (Fig. 3H, J), then determined the ratio between the invasion area and the core area (Fig. 3J). DCA increased this ratio after 13 days in culture, indicating that it increased cell detachment and mobility in 3D structures. The addition of OA did not affect the core size of the spheres (Fig. 3K). However, it strongly increased the invasion/core ratio, especially in the presence of DCA (Fig. 3L), suggesting the involvement of lipid metabolism.

DCA-induced metabolic rewiring is associated with increased expression of stress ligands on tumor cells, recruitment of NK cells and sensitization to NK cells

We recently showed that DCA increases the expression of genes encoding NK cell-activating ligands in leukemic cells(41). As mentioned above, in 2D culture conditions, DCA also able to increased *MICA, MICB, ULBP1 and ULBP4* in HCT116 cells (Fig. 2I). *ICAM-1* expression also increased. Consistent with these transcriptional changes, flow cytometric analysis demonstrated an increased surface expression of stress ligands following DCA treatment. Importantly, inhibition of fatty acid oxidation with etomoxir partially reversed this induction, indicating that FAO contributes to DCA-mediated stress ligand expression. Similar results were obtained in MDA-MB-231 breast cancer cells (Supplemental Fig. 2B-C).

Hence, FAO induces the expression of a pattern of ligands that should favor NK cell recognition and NK cell-mediated elimination. Furthermore, DCA induced stress ligand expression in both spheroids and detached cells (Fig. 3D-E). Hence, we analyzed whether DCA favored NK cell recognition by tumor cells. First, we incubated CTFR-stained *in vitro* expanded and activated NK cells (eNK) with HCT116 spheroids for 48h, harvested the spheroids and surrounding medium separately, and analyzed the cells by flow cytometry (Fig. 4A). DCA increased NK cell infiltration in spheroids (Fig. 4A1). As expected, a reduction in the non-infiltrate fraction was observed (Fig. 4A2). To visualize NK cell infiltration, we stained HCT116 spheroids with calcein before adding the CTFR-stained eNK cells. DCA-treated spheroids showed a significant increase in NK cell infiltration (Fig. 4B-C). We also used automated microscopy Cytation®, which confirmed that DCA promoted eNK to deeply infiltrate the spheroids (Supplemental Fig. 3A). This was even more evident when spheroids formed from MDA-MB-231 cells (Supplemental Fig. 3B). As DCA recruited eNK towards the spheroids, we investigated if it could favor tumor cell destruction. In 2D, DCA did not significantly increase eNK cytotoxicity (Fig. 4D). However, in 3D DCA and eNK separately reduced spheroid area and when used together they significantly reduced it further (Fig. 4E). Notably, DCA did not reduce the surrounding (halo) area, which mainly comprised eNK (Fig. 4F). Supplemental Fig. 4A shows that eNK cells moved to the center of the well in the absence of spheroids. To exclude the possibility that eNK moved to the spheroids due to gravity, we placed the spheroids out of the well center (Supplemental Fig. 4B). We observed that eNK cells actively moved towards the spheroid. This showed that NK cells infiltrated the spheroids, which was further enhanced upon DCA treatment.

FAO increases metastasis in a zebrafish model

We have shown in several *in vitro* models that DCA induces EMT in cancer cells, facilitating their migration and invasion. To assess this property in vivo, we chose zebrafish as a suitable model (44), enabling the investigation of cell motility at the level of individual cells in a longitudinal context. We used the MDA-MB-231 cell line because of its invasiveness and aggressiveness (38), and evaluated metastasis by counting the number of fish in which cells were observed in the zebrafish body away from the injection site (periyolk space), specifically in the tail, at various time points. Epifluorescence images obtained after in vivo monitoring at 24, 48, 72, and 120 hours post injection (hpi) allowed us to determine the effect of DCA on cell invasion properties (Fig. 5A-D). DCA-treated MDA-MB231 xenografted cells

were observed in the tail in more than 80% of fish at 24hpi, compared to only 57% of untreated cells at the same time point (Fig. 5A-B). However, at 120hpi, we did not observe statistical differences, as the fraction of invasive cells in non-treated fish increased progressively to reach 100% under both conditions (Fig. 5B). Hence, to study drug effects on motility, we focused in relative short time periods before engrafted cells naturally colonize the host. High-resolution images showed single-cell migration to the perivascular caudal region at 24hpi (Fig. 5A, D). In DCA-treated cells, invasive cells were more numerous at the periphery of the dorsal longitudinal anastomotic vessel (DLV) and posterior cardinal vein (PCV) in the zebrafish caudal region than in non-treated cells. Moreover, we noticed that DCA pretreated cells were more dispersed after injection than non-treated cells (Fig. 5D). To assess whether FAO enhances the number of migrating cells, we measured the area of the invading cells (Fig. 5C). At 24hpi, the mean area tended to increase in the DCA-treated condition compared to than in the non-treated condition, although this effect was lost at later time points.

FAO sensitized tumor cells to NK cell-induced killing in vivo

To investigate whether metabolic changes sensitized tumor cells to NK cell-mediated killing, we treated MDA-MB231 cells with DCA and engrafted them as shown in Fig. 5 alongside eNK cells in zebrafish. DCA-treated tumor cells exhibited increased presence in the tail region. eNK migrated through the vascular system of the zebrafish larvae and successfully reached the tail (Supplemental Fig. 5A). In the presence of eNK cells, there was a significant reduction in the number of tumor cells reaching the tail, effectively preventing tumor cell invasion in this area (supplemental Fig. 5B). We quantified the CTFR fluorescence intensity in the tail as a readout of tumor cell invasion. NK cell effects were more apparent in DCA-treated cells (Supplemental Fig. 5B). To compare the effect of NK cells on control cells versus DCA-treated cells, the fluorescence intensity in non-eNK treated fish was set to 100 (Fig. 6). This enabled the comparative analysis, revealing that eNK cells were more effective on preventing the DCA-treated MDA-MB231 cells to reach the tail than on non-treated cells (Fig. 6B).

DCA favors metastasis formation in mice

To further assess the ability of DCA to promote metastasis, we orthotopically engrafted 4T1 cells into the mammary fat

pad of athymic nude fox n1 mice. In this 4T1 model, engrafted cells migrate to the lung generating visible metastasis

that can be quantified because they are not stained with Indian ink and appear as white dots in the lung (Fig. 7A). DCA

was administered by oral gavage to ensure optimal bioavailability. Athymic nude fox n1 mice lack functional T and B

cells but retain NK cells (39). DCA did not affect mice weight or primary tumor volume (Supplemental Fig. 6A). Visually, the effect of DCA on the number of lung metastasis was unclear (Fig. 7A, left). Quantification showed that DCA treatment did not induce a statistically significant change in the average number of metastasis in these mice (Fig. 7B, left).

We subsequently conducted a second experiment using NOD-scid IL2rγ$^{-/-}$ (NSG / NOD-SCID-γ) mice (supplemental

Figure 6B), which lack NK cells in addition to being devoid of T and B cells (45, 46). Again, DCA did not alter body weight, behavior, or primary tumor volume (Supplemental Fig. 6B). In the absence of NK cells, lung metastasis increased by a factor of 10 (Fig. 7B, compare y axes in left and right), supporting the essential role of this lymphocyte lineage in metastasis immune surveillance as discussed earlier. Moreover, visual inspection of lungs showed that DCA clearly increased the number of metastasis/lung (Fig. 7A, right). Quantification revealed a statistically significant increase in the average number of metastasis per lung lobe in the presence of DCA (Fig. 7B, right). Therefore, NK cells can, at least partially, decrease the pro-metastatic effect of DCA.

Together, these results demonstrate that DCA enhances cell motility and metastatic dissemination in two complementary in vivo models, and that the presence of NK cells counteracts the pro-metastatic potential of DCA.

Discussion

FAO, which fuels β-oxidation and mitochondrial respiration, is strongly associated with tumor progression, invasion, and metastasis (5, 6).To sustain elevated FAO, metastatic cells increase fatty acid import and activate multiple FAO-related genes, notably CD36 (4, 6). Our findings show that artificially stimulating FAO through DCA induces motility, invasion, EMT-associated transcriptional programs, and mesenchymal marker expression, supporting the idea of a reciprocal reinforcement between FAO and EMT (Fig. 8). Importantly, pharmacological inhibition of FAO with etomoxir partially reversed the DCA-induced changes in EMT markers, providing functional evidence that FAO actively contributes to the acquisition of the mesenchymal phenotype rather than merely accompanying it (Fig. 8; Supplemental Fig. 2A-C).

A notable observation from our study is that DCA significantly decreased intracellular levels of two major saturated fatty acids, palmitic acid (C16:0) and stearic acid (C18:0), in HCT116 cells; with a concomitant accumulation of neutral lipids, as revealed by BODIPY staining using both immunofluorescence microscopy and flow cytometry. Although at first glance these results might seem contradictory, they align well with the metabolic adaptations described in FAO-driven cancer cell plasticity. Several studies have shown that FAO activation accelerates the consumption of free saturated fatty acids, including palmitate and stearate, which are preferential substrates for β-oxidation (47–51). Simultaneously, increased FAO produces an excess of acyl-CoA molecules that cells must buffer to avoid lipotoxicity. Cancer cells typically manage this stress by channeling fatty acids into triglyceride synthesis and storing

them within lipid droplets, leading to an overall accumulation of neutral lipids (48, 50).Thus, the depletion of free palmitic and stearic acids likely reflects their rapid use as substrates for FAO, whereas the increase in neutral lipids reflects compensatory lipid droplet formation. DCA also stimulates mitochondrial biogenesis and cell mass, leading to cellular hypertrophy (52). Thus, even though the total amount of neutral lipids increases, lipid density (lipid fluorescence signal normalized to cell surface area or volume) does not increase, because the enlargement of the cell dilutes the increase in lipid content. This coordinated remodeling of lipid pools is characteristic of FAO-driven metabolic states associated with EMT, enhanced migration, and metastatic competence (53, 54).

It is well-known that metastatic cells increase their motility, rely more heavily on FAO and become more susceptible to NK cell surveillance. We show here that FAO promotes the expression of NK-activating ligands, thereby enhancing NK-mediated tumor cell killing. Importantly, pharmacological inhibition of FAO partially reversed the DCA-induced increase in stress ligand expression in HCT116 cells and showed the same trend in MDA-MB-231 cells, indicating that FAO directly contributes to the acquisition of this immunogenic phenotype across distinct tumor types. This effect was consistently observed in 3D matrices and in zebrafish xenografts but was considerably weaker in 2D cultures. The discrepancy likely arises from structural and biophysical differences between 2D monolayers and 3D environments. Extracellular matrix composition, cell–cell contacts, mechanical constraints, and cytokine diffusion differ greatly between these contexts and are known to facilitate immune synapse formation and NK recruitment in 3D structures (*55*). Similar matrix-dependent modulation of NK activity has been reported in several cancer models (56).

In both 2D and 3D settings, FAO induction through DCA increased the expression of the activating ligand PVR (CD155), a nectin-like adhesion molecule involved in adhesion, proliferation, migration, and immune regulation (57, 58). PVR interacts with both activating and inhibitory NK receptors, including CD226/DNAM-1 (58, 59), TIGIT, and CD96 (60), and is often overexpressed in aggressive tumors (61). We also found that FAO reduced the expression of E-Cadherin (CDH1) and MHC-I, two inhibitory ligands recognized by KLRG1 and KIRs, respectively (11, 16). In addition, FAO increased ULBP4 in 3D cultures and ULBP1/MICA/B in 2D cultures, all of which serve as ligands for the activating receptor NKG2D (15). NK cell engagement depends on the integration of multiple activating and inhibitory signals (62, 63), and because the loss of E-Cad/KLRG1 interaction alone does not restore NK cytotoxicity (11), it is unlikely that one ligand alone mediates FAO-induced NK sensitization. Instead, our data support the emergence of a combinatorial ligand “pattern” driven by FAO, which may vary among cancers and patients and could contribute to the heterogeneous clinical response to DCA (29, 64).

In our model we have used expanded and activated NK cells (eNK), which have a different metabolic profile than naïve NK cells. However, it should be noted that peripheral blood NK cells once are recruited close to the tumor should start their activation and/or will be quickly activated once infiltrating the tumor environment or by encountering the tumor target cell. Therefore, the use of activated NK cells could reflect the physiological context. In addition, in cancer patients peripheral blood NK cells could contain NK cells that have already been in contact with the tumor cells, and are indeed activated. This has been

unveiled for example by the presence of tumor molecules in NK cells by the process of trogocytosis (65, 66).

In the zebrafish model, DCA-pretreated cells displayed enhanced motility during the first 24 hours, after which the effect waned. DCA is rapidly metabolized, which may limit its long-term influence on cancer cell behavior in vivo. Moreover, DCA reduced proliferation, leading to fewer cells at later time points compared with controls. By 72 hours, virtually all injected cells had disseminated throughout the host, regardless of treatment, making any early differences in migration less distinguishable. These transient effects are consistent with other studies describing the time-dependent metabolic and migratory changes induced by DCA (67).

Nude mice, despite lacking T cells, retain functional NK cells (39). In contrast, NSG mice lack NK cells and therefore cannot exert NK-mediated immunosurveillance (48, 69). Consequently, the pro-metastatic effects of DCA, driven by FAO induction and EMT, were more apparent in NSG mice, where they were no longer counterbalanced by NK-cell surveillance. These results are consistent with the well-established role of NK cells as critical regulators of metastatic seeding and outgrowth (12, 70) and support the idea that FAO exposes a metabolic vulnerability that can be exploited by NK cells. Indeed, our findings suggest that DCA simultaneously promotes tumor cell dissemination while increasing tumor susceptibility to NK-cell recognition, resulting in two opposing effects whose relative contribution depends on the presence or absence of NK cells.

ERK5 is a good candidate to play a central role as regulator of EMT, FAO, and immune recognition (33, 35, 68). Targeting ERK5 or FAO-related components such as CD36 (10, 69) may provide therapeutic benefits, particularly given that CD36 overexpression promotes metastasis and correlates with poor prognosis across multiple cancer types (6, 7, 70, 71). DCA has shown inconsistent clinical efficacy (64), and although its ability to induce oxidative metabolism and sensitize cancer cells to NK cell killing is intriguing, its pro-migration and pro-invasion effects raise concerns, especially at doses higher than those typically used clinically. Nonetheless, metabolic rewiring as a strategy to enhance NK activation remains promising. Metformin, for instance, can sensitize tumors to NK cells by increasing ICAM-1 expression (27). Drugs targeting metabolic pathways to modulate NK–tumor interactions may represent an emerging class of immunotherapies (22, 25), and our results provide a conceptual and methodological framework to identify such compounds.

In conclusion, during EMT and metastatic progression, tumor cells rely heavily on FAO and this metabolic program induces a distinctive pattern of NK-recognizable ligands. This suggests the existence of an Achilles' heel in metastatic cells, which may be exploited by therapies that enhance NK surveillance or modulate tumor cell metabolism.

Methods

Cell culture and transient transfections

The colon carcinoma HCT116 (gift from SIRIC Montpellier) and the triple negative breast cancer MDA-MB231 cell lines were cultivated in 75cm2 flasks (Corning) in DMEM Glutamax containing Glucose (4.5g/L), pyruvate (0.11g/L) and 10% Fetal Bovine Serum (without antibiotics). Cell number, viability and death were analyzed using a Muse Cell Analyzer (Millipore) by incubating cells with Muse Count & Viability and Annexin V and Dead Cell kits respectively, following the manufacturer's instructions. Absence of mycoplasma in the medium is checked monthly.

For cell transfection, 2 million HCT116 cells were plated, and after 48 h they reached 80% confluency. Then, 300 µl of Opti-MEM (Invitrogen) was taken separately in two 5ml polypropylene tubes for each condition and 40 µl of Lipofectamine 2000 transfection reagent RNAiMAX (Invitrogen) was added to one of them and 12 µl of siRNA (20µM) was added to another tube for each condition following the manufacturer's protocol. All siRNAs, that is siCD36, siERK5 and siControl were ON-TARGETplus SMARTpools (mixture of 4 siRNA) from Dharmacon. The cells were then analyzed after 48 h.

Cell Migration Assay

Cells ($25x10^3$ in 200 µl of medium without FBS) were seeded in the top chamber (insert) of 24-well transwell plates (Corning), and treated with 10mM DCA and/or 3µM OA. The outer chambers contained 700µl of the same conditioned medium with 10% FBS, except for the negative control, which did not contain FBS. This treatment was repeated at 24 h. At 48h, the medium was removed from both the insert and well. The inserts were washed twice with 1 x PBS, and cells were fixed in 4% paraformaldehyde (PFA) for 10 min. The cells were stained with crystal violet (24 h) and washed twice with 1X PBS. Staining from the upper layer of the well was removed using a cotton-tipped applicator and the inserts were allowed to dry. Finally, the lower layer (cells that reached the underside of the insert) was analyzed under a microscope and pictures were taken before analyzing the number of colonies.

RT-QPCR experiments

Total RNA was extracted using NucleoSpin RNA isolation columns (Macherey-Nagel), reverse transcription was carried out using the iScript™ cDNA Synthesis Kit (Bio-Rad) and 100µL of RNAse free water was added to the 20µl sample. Two µl of each sample were analyzed in a light cycler 480 Roche. All samples were analyzed using the 2 (-DDCt) method and normalized to *β-actin* mRNA levels.

Mito stress test (Seahorse XF)

Agilent Seahorse XF96 Cell Culture Microplates were pre-coated with poly-d-lysine. Then $7,5x10^3$ HCT116 cells were seeded in regular growth medium and treated with 5mM DCA and/or 3µM OA. The medium was changed after 24h and cells analyzed at 48h. Thirty minutes before the analysis, the seahorse was calibrated for the Mito stress test. The microplates were loaded and analyzed for 90 min. The oxygen consumption rate was determined using an XFe/XF analyzer.

Immunoblotting

Samples were collected, washed with PBS and lysed in RIPA buffer. Protein concentration was determined by BCA assay (Pierce) before denaturation and electrophoresis on 4–15% TGX gels (BioRad). Protein transfer was performed using a TransTurbo system (Bio-Rad) on nitrocellulose membranes (Bio-Rad). After blocking for 1 h with 5% non-fat milk, the membranes were incubated overnight at 4°C in agitation with primary antibodies, washed three times with PBS-Tween 0.1% and incubated with the appropriate HRP-labeled secondary antibody for 1 h. Membranes were washed out three times with PBS-Tween 0.1% and developed with Substrat HRP Immobilon Western (Millipore). Band quantification was performed using the “ImageLab” software from BioRad and represented as the ratio between the protein of interest and a control protein i.e. actin or tubulin. The value of 1 is arbitrarily given to control cells. Anti-CD36 antibody was from Gentex (GTX112891). EMT related protein antibodies were from the EMT antibody sampler kit (Cell Signaling, #9782). The antibody against β-Actin and HRP-labeled secondary antibodies were from Sigma.

Immunofluorescence

Thirty-thousand HCT116 cells were seeded on coverslips into 6-well plates and treated for 48h with sterile water (vehicle) or 5 mM DCA and/or 3µM OA. On the third day, the medium was removed and each well was washed with PBS. Then the cells were fixed in 4% PFA for 15 minutes at RT. After fixation, cells were incubated at RT for 15 minutes with an anti-CD36 antibody (CD36-PE clone REA760, Miltenyi; 1/100) and washed twice with PBS. Then, they were incubated for 15 minutes with DAPI (1/1000) and washed twice with PBS. After mounting the slides, they were dried in the dark for at least 2 days at 4°C and analyzed with a Leica Sp8 microscope.

Neutral lipids levels (Bodipy)

It was basically performed as previously described (72). For immunofluorescence analysis, HCT116 were seeded on poly-D-lysine coated coverslips at day 0 and treated with 5mM DCA and/or 3µM OA for 48h. Cells were fixed with 4% PFA, and stained with Bodipy (2µM, 15min at 37°C) and DAPI. Images were taken with a Sp8 Leica microscope.

For lipid quantification by flow cytometry, HCT116 cells were seeded at $1x10^6$ cells in 10 cm dishes and treated with 5mM DCA and 30µM OA for 48h. Cells were incubated with Bodipy for 15 minutes, wash with PBS and harvested after trypsinization. After centrifugation, cells were resuspended in PBS and analyzed in a Gallios Flow cytometer (Beckman). Results were analyzed with Kaluza Software.

Neutral lipids/cell surface

Cells were seeded at 3,000 cells per well in 96-well µClear black plates (PS, F-bottom chimney well; Cellstar, ref. 655090, lot E23033LG) and cultured for 48 h in the presence of DCA, 10 mM) and oleic acid (OA, 30 µM).

On Day 2, cells were fixed in 4% PFA and permeabilized with 0.01% Triton X-100. Lipid droplets were stained with BODIPY™ 558/568 C12 (ThermoFisher, 1:2000), F-actin with Alexa Fluor™ 647–647-phalloidin (ThermoFisher, 1:5000) for 45 min, and nuclei with Hoechst (1: 10,000, 3 min).

High-content imaging was performed on an Opera spinning disk confocal system (PerkinElmer) using standard excitation/emission settings. Image segmentation and quantitative feature extraction were carried out in Harmony® (PerkinElmer) using built-in algorithms for nuclei, cytoplasm, and lipid droplet detection.

Metabolomic Analysis

HCT116 cells were treated for 48 h with DCA (1, 5, and 10 mM). After trypsinization and centrifugation, pellets were resuspended in 250 µL Milli-Q water and homogenized. Aliquots (100 µL) were used for NL_AGT and total fatty acid analyses; the remainder for protein quantification.

Neutral lipids were extracted using the Bligh and Dyer method (1959) with internal standards (stigmasterol, cholesteryl heptadecanoate, glyceryl trinonadecanoate). Extracts were analyzed by GC-FID (Trace 1600, Thermo Electron) on an RTX-5 column (5 m × 0.25 mm, 0.25 µm; 190–350°C, 5°C/min; H_2 5 mL/min) (Barrans et al., 1994).

Lipid residues were hydrolyzed (0.5 M KOH/methanol, 55°C, 30 min), transmethylated (14% BF_3/methanol, 80°C, 1 h), and extracted with heptane. FAMEs were analyzed by GC-FID (Trace 1300, Thermo Fisher) using a Famewax RESTEK column (30 m × 0.32 mm, 0.25 µm; 100–250°C, 6°C/min; H_2 1.5 mL/min) (Lillington et al., 1981).

Flow Cytometry

Briefly, 1 × 10^6 cells were stained with the appropriate antibodies in PBS, 2% FBS and incubated at 4°C for 20 min. Cells were then washed and suspended in 200–250 µl of PBS and 2% FBS and the staining was analyzed using a Gallios flow cytometer (Beckman) and its Kaluza software.

NK cell expansion and culture (eNK)

NK cells were expanded from patient umbilical cord blood according to the protocol developed by our team (73, 74) and then cultivated in RPMI 1640 GlutaMAX™ + 10% FBS, at 37°C with 5% of CO2 until use. eNK cells were counted with the Muse® Cell Analyzer.

eNK labeling

eNK cells were labeled for 20min with CellTrace™ Far Red in RPMI 1640 GlutaMAX™ without serum, washed with RPMI 1640 GlutaMAX™ + 10% FBS and suspended in complete spheroid medium. They were seeded with the spheroids at a ratio effector: target of 1:1 and incubated at 37°C with 5% of CO_2 in the AgilentBioTek BioSpa 8 to begin the imaging kinetic.

eNK cell infiltration by flow cytometry

One thousand HCT116 cells were resuspended in serum-free medium containing 1µM Calcein-AM (Invitrogen®, ref. C1430) for 4 h at 37°C. Spheroids were formed into U-plate ultra-low attachment cluster 96 well round bottom plates (Corning® Costar®, 7007) and grown for 2 days, then treated with 10mM DCA for 2 additional days. On day 5, NK cells stained with CellTrace™ FarRed (Invitrogen®, ref.

C34564, 1:3000 dilution) following the provider's instructions and added to the HCT116 spheroids at E:T ratio 1:1. Next day, the spheroids and their supernatants were pooled together. After sedimentation of the spheroids, the supernatants are collected separately. Both were prepared for flow cytometry analysis.

Spectral flow cytometry for EMT and Stress ligands panel

HCT116 and MDA-MB-231 cells were seeded at $1x10^5$ cells per well in 24-well plates. The following day, cells were treated with 10 mM DCA, 10 µM etomoxir, or both for 24 or 48 h. Three independent experiments were performed at 24 h and four at 48 h. Cells were detached using TrypLE to preserve surface proteins, and viability was assessed using Fixable Viability Dye eFluor 780 (Invitrogen). Three separate staining tubes were prepared for each condition. The EMT surface tube contained E-cadherin VioBright V423 (clone REA811, Miltenyi Biotec, 1:200) and N-cadherin APC (clone 8C11, 1:200). The intracellular EMT tube was fixed and permeabilized for 20 min at 4°C, washed with Perm/Wash buffer, and stained with vimentin PE (clone REA409, Miltenyi Biotec, 1:200). The stress-ligand tube contained MICA/B APC (clone REA1076, Miltenyi Biotec), ULBP4 PE (clone 709116, R&D Systems) and ULBP2/5/6 Alexa Fluor 405 (clone 165903, R&D Systems), each used at 1:200. Samples were acquired on a Cytek Northern Lights spectral flow cytometer and analysed using SpectroFlo software. Debris, doublets and non-viable cells were excluded before analysing marker expression within the live singlet-cell population.

Spheroid formation

Four hundred HCT116 or MDA MB 231 cells were seeded in U-plate ultra-low attachment cluster 96 well round bottom (Costar, #7007) plates in 200µL of DMEM/F12 media supplemented with B27 (Invitrogen), 20ng/mL EGF (Peprotech), 10ng/mL β-FGF (Peprotech) and 5µg/mL of human insulin (Peprotech). Plates were then centrifuged twice (opposite sides) without brakes at 400g. Spheroid formation was followed daily under a Zeiss microscope.

Spheroids in Geltrex™

Spheroids were formed in ULA and transferred into a Falcon® 96-well Clear Round Bottom plate (one per well) by pipetting 20µL of medium containing the spheroid with P200 tips. Geltrex™ was diluted in cold PBS to obtain a 7% solution and 100µL were added on the transferred spheroids to resuspend them. The plate was centrifuged for 5min at 4°C, 300g, to eliminate bubbles. Then it was incubated at 37°C in 5% CO2 for 30-45min to polymerize the gel. Once Geltrex™ polymerized, 100µL of complete spheroid medium was added, directly on the gel, with the different treatments: H_2O (control), 3µM OA and/or 10mM DCA (dissolve in H_2O). Treated spheroids were incubated at 37°C with 5% CO_2 and treatments were renewed every day and invasiveness measured as previously described (75).

Spheroid Imaging

The 96-well plate containing spheroids in Geltrex™ 7% were imaged daily with the Agilent BioTek Cytation 5. eNK co-culture imaging kinetic was realized automatically by the association of the BioSpa and the Cytation 5. The plate was transferred between the tools by a robotic arm every 2 hours.

Measures of the spheroid core and invasive area

The measures of the spheroid core and invasive area (Example Fig. 5C) were performed on the Agilent BioTek Gen5 software and reported on an Excel spreadsheet. The invasiveness was calculated by the ratio between the spheroid area and the invasive area.

Mouse experiment

4T1-luciferase breast cancer cells tested pathogen-free were cultured under standard conditions, harvested at ~ 60% confluency, washed, and suspended in PBS before orthotopic injection of 1×10^6 cells into the fourth mammary fat pad of 7-week-old female mice. Athymic nude fox n1 mice (n = 20) or NOD SCID-g mice (n = 14) were randomly assigned into two groups receiving either DCA (100 mg/kg/day in water, oral gavage monday–friday) or vehicle alone, beginning the day after implantation and continuing for 17 days to treatment groups, and treatments were administered without blinding. Mice were weighed every 2 days and tumor volume was measured using a Caliper. After 3 weeks of treatment, mice were sacrificed by cervical dislocation and tumors were extracted and measured. Lungs were injected with a needle through the trachea with a solution of 15% Indian ink in distilled water, until the lungs were completely swollen. Black swollen lungs were then extracted from the mice and fixed using Fekete's solution (40 ml of glacial acetic acid, 80 ml of 37% Formalin, 580 ml of (100%) ethanol and 200 ml of water). Metastases in the lung were observed as white (non-colored) dots and the different lobes were dissociated to accurately count the number of metastases in each lobe. Data were evaluated using two-way ANOVA for longitudinal measurements and unpaired t-tests or Mann–Whitney tests for endpoint comparisons, with $p < 0.05$ considered significant. All animal experiments were conducted in accordance with French regulations and were approved by the relevant French authorities under protocol number APAFIS #23071-2019112714372794 v4.

Zebrafish in-vivo assay

For *in vivo* metastasis assay, MDA-MB231 cells were treated for 72h with 10mM DCA and labeled with 5µM CTFR (Thermofisher). Four hundred cells were injected in the perivitelline space of 48hpf (hours post-fertilization) zebrafish embryo after being anesthetized with MS-222 (200 mg/l, Sigma-Aldrich) and maintained at 33°C. A total of 32 fish were used for both conditions (n = 32). DCA effects were assessed at 24, 48, 72 and 120hpi (hours post-injection) using epifluorescence microscopy (inverted confocal microscope TCS SP5, Leica systems). The area of invading cells was measured using Fiji software (44, 76).

For high-resolution imaging, 400 CTFR-labeled MDA-MB231 cells were injected into the perivitelline space of Tg(Kdrl:egfp) transgenic zebrafish line with fluorescent vasculature. At 48hpf zebrafish embryos were placed on glass-bottom petri dishes and covered with methylcellulose containing 0.003%

tricaine (Sigma-Aldrich). Images were acquired using a Leica SP8 confocal microscope (Leica Microsystems).

Cytotoxic assay of eNK cells in zebrafish

We injected eNK alongside the cancerous MDA-MB231 cell line into the perivitelline space of 48hpf zebrafish embryos. MDA-MB231 cells were pre-treated with DCA for 72 hours prior and then labeled with CTFR and suspended at a concentration of 80 × 10^6 cells/mL to inject 4nL in embryos (200 cells/embryo). For the SDH-mAb arming, eNK cells were armed with SDH-cetuximab or SDH-rituximab by incubating them with 10 µg/mL of these mAbs for one hour at 37°C with 5% CO_2 as previously described (77). The eNK were labeled with Violet Cell Trace and injected at an effector-to-target ratio of 5:1 into the perivitelline space of 48hpf embryos. Imaging was performed using an epifluorescence microscopy. The program Fiji was used to measure the mean fluorescence intensity of cells in the tail of the zebrafish embryos at 48hpi.

Statistical analysis:

All statistical analyses were performed using GraphPad Prism version 9 (GraphPad Software, San Diego, CA, USA). Unless otherwise indicated, data are presented as mean ± standard deviation (SD) from at least three independent biological experiments. The number of independent experiments (n) or biological replicates analyzed is specified in the corresponding figure legends.

For comparisons involving more than two groups, statistical significance was assessed using one-way ANOVA followed by Tukey's multiple-comparison test. For spheroid growth and invasion kinetics involving multiple independent comparisons, multiple unpaired t-tests with Holm–Šídák correction for multiple testing were applied. Comparisons between two independent groups were performed using an unpaired Student's t-test, whereas paired t-tests were used when measurements were obtained from matched samples (e.g., NK-cell donor experiments). When data did not meet the assumptions of parametric testing, comparisons were performed using the Mann–Whitney U test. Longitudinal measurements, including tumor growth, were analyzed using two-way ANOVA, whereas categorical variables, such as the proportion of zebrafish presenting metastatic dissemination, were analyzed using the chi-square test.

Statistical significance is indicated as follows: $P < 0.05$ (*), $P < 0.01$ (**), $P < 0.001$ (***), and $P < 0.0001$ (****).

Declarations

Competing interests

The authors declare no competing interests.

Competing interests

The authors declare no competing interests.

Funding

This work was supported by INCA/DGOS PRT-K program 2021-014 (MV), by INCA PLBio 2021-069 (GB/MV) and PLBIO23-028 (DF/MV), the “Investissements d’avenir” Grant LabEx MAbImprove: ANR-10-LABX-53 (MV), the 2021 AAP Companies On Campus by the MUSE “Montpellier Université d’Excellence” (MV). LC is a recipient of a fellowship from MRT and M.C-M. of the ARC, France. La Fondation Bristol Myers Squibb pour la Recherche en Immuno-oncologie 2025–2026.

Author contributions

S.Z., M.V. and D.G. participated in the research design. S.Z., S.E., B.H., A.B., C.A., C.J., N.D., A.S., J.P., M.D.T., and D.G. conducted the experiments. M.C and N.A-V provided fresh eNK cells. All authors contributed to data analysis, discussions and interpretation. G.B., A.A., M.V and D.G. supervised the study and drafted the paper. All authors read and approved the paper.

Acknowledgements

This work was supported by the grant from the French National Research Agency (ANR) for the "PEPR iCHONDRO" project (ANR-22-PEBI-0002). We acknowledge the imaging facility MRI, member of the national infrastructure France-BioImaging supported by the French National Research Agency (ANR-/10-INBS-04, «Investments for the future») for the access to the cytometry platform. This work was supported by the “Investissements d’avenir” Grant LabEx MAbImprove: ANR-10-LABX-53 (GC/MV/PM/BR). We acknowledge the support of Immun4Cure IHU "Institute for innovative immunotherapies in autoimmune diseases" (France 2030 / ANR-23-IHUA-0009).

La Fondation Bristol Myers Squibb pour la Recherche en Immuno-oncologie, Laureat 2025 (MV).

Lipidomic analysis were performed at MetaToul (Toulouse metabolomics & fluxomics facilities, www.mth-metatoul.com on the site dedicated to Lipids Analysis Inserm I2MC) and was supported by the MetaboHUB infrastructure funded by the Agence Nationale de la Recherche under the France 2030 program (MetaboHUB ANR-11-INBS-0010 ; MetEx + ANR-21-ESRE-0035; MetaboHUB (JVCE) ANR-24-INBS-0012

We acknowledge the imaging facility MRI, member of the national infrastructure France-BioImaging supported by the French National Research Agency (ANR-/10-INBS-04, «Investments for the future») for the access to the cytometry platform and Gallios 3 Lasers cytometer. We acknowledge the tissue engineering facility CARTIGEN supported by the “FEDER/Region Occitanie” program, CHU Montpellier and the University of Montpellier for providing access to the Symphony A3 Cytometer. Umbilical cord blood units (UCBs) were obtained from the Biological Resource Center Collection of the University Hospital of Montpellier - (BIOBANQUES Identifier - BB-0033-00031, CHU Montpellier).

We thank Drs. Nerea Allende-Vega and Loïs Coenon for providing fresh eNK cells when needed for the project.

References

1. P. P. Hsu, D. M. Sabatini, Cancer cell metabolism: Warburg and beyond. *Cell* 134, 703–707 (2008).
2. A. Carracedo, L. C. Cantley, P. P. Pandolfi, Cancer metabolism: fatty acid oxidation in the limelight. *Nat. Rev. Cancer* 13, 227–232 (2013).
3. J. Massagué, A. C. Obenauf, Metastatic colonization by circulating tumour cells. *Nature* 529, 298–306 (2016).
4. J. Wang, Y. Li, CD36 tango in cancer: signaling pathways and functions. *Theranostics* 9, 4893–4908 (2019).
5. Z. Li, Y. Kang, Lipid Metabolism Fuels Cancer’s Spread. *Cell Metab.* 25, 228–230 (2017).
6. G. Pascual, A. Avgustinova, S. Mejetta, M. Martín, A. Castellanos, C. S.-O. Attolini, A. Berenguer, N. Prats, A. Toll, J. A. Hueto, C. Bescós, L. Di Croce, S. A. Benitah, Targeting metastasis-initiating cells through the fatty acid receptor CD36. *Nature* 541, 41–45 (2017).
7. A. Ladanyi, A. Mukherjee, H. A. Kenny, A. Johnson, A. K. Mitra, S. Sundaresan, K. M. Nieman, G. Pascual, S. A. Benitah, A. Montag, S. D. Yamada, N. A. Abumrad, E. Lengyel, Adipocyte-induced CD36 expression drives ovarian cancer progression and metastasis. *Oncogene* 37, 2285–2301 (2018).
8. Y. Tang, J. Zhou, S. C. Hooi, Y.-M. Jiang, G.-D. Lu, Fatty acid activation in carcinogenesis and cancer development: Essential roles of long-chain acyl-CoA synthetases. *Oncol. Lett.* 16, 1390–1396 (2018).
9. J. Quan, C. Cheng, Y. Tan, N. Jiang, C. Liao, W. Liao, Y. Cao, X. Luo, Acyl-CoA synthetase long-chain 3-mediated fatty acid oxidation is required for TGFβ1-induced epithelial-mesenchymal transition and metastasis of colorectal carcinoma. *Int. J. Biol. Sci.* 18, 2484–2496 (2022).
10. R. Sánchez-Martínez, S. Cruz-Gil, M. Gómez de Cedrón, M. Álvarez-Fernández, T. Vargas, S. Molina, B. García, J. Herranz, J. Moreno-Rubio, G. Reglero, M. Pérez-Moreno, J. Feliu, M. Malumbres, A. Ramírez de Molina, A link between lipid metabolism and epithelial-mesenchymal transition provides a target for colon cancer therapy. *Oncotarget* 6, 38719–38736 (2015).
11. P. J. Chockley, J. Chen, G. Chen, D. G. Beer, T. J. Standiford, V. G. Keshamouni, Epithelial-mesenchymal transition leads to NK cell-mediated metastasis-specific immunosurveillance in lung

cancer. *J. Clin. Invest.* 128, 1384–1396 (2018).

12. S. Lorenzo-Herrero, A. López-Soto, C. Sordo-Bahamonde, A. P. Gonzalez-Rodriguez, M. Vitale, S. Gonzalez, NK Cell-Based Immunotherapy in Cancer Metastasis. *Cancers* 11, 29 (2018).
13. G. G. Bushnell, D. Sharma, H. C. Wilmot, M. Zheng, T. D. Fashina, C. M. Hutchens, S. Osipov, M. Burness, M. S. Wicha, Natural Killer Cell Regulation of Breast Cancer Stem Cells Mediates Metastatic Dormancy. *Cancer Res.* 84, 3337–3353 (2024).
14. H. Tsuchiya, G. Shiota, Immune evasion by cancer stem cells. *Regen. Ther.* 17, 20–33 (2021).
15. S. Duan, W. Guo, Z. Xu, Y. He, C. Liang, Y. Mo, Y. Wang, F. Xiong, C. Guo, Y. Li, X. Li, G. Li, Z. Zeng, W. Xiong, F. Wang, Natural killer group 2D receptor and its ligands in cancer immune escape. *Mol. Cancer* 18, 29 (2019).
16. M. A. Sartor, V. Mahavisno, V. G. Keshamouni, J. Cavalcoli, Z. Wright, A. Karnovsky, R. Kuick, H. V. Jagadish, B. Mirel, T. Weymouth, B. Athey, G. S. Omenn, ConceptGen: a gene set enrichment and gene set relation mapping tool. *Bioinforma. Oxf. Engl.* 26, 456–463 (2010).
17. A. Dongre, M. Rashidian, F. Reinhardt, A. Bagnato, Z. Keckesova, H. L. Ploegh, R. A. Weinberg, Epithelial-to-Mesenchymal Transition Contributes to Immunosuppression in Breast Carcinomas. *Cancer Res.* 77, 3982–3989 (2017).
18. I. Filip, A. Wang, O. Kravets, R. Orenbuch, J. Zhao, T. E. Perea-Chamblee, G. A. Manji, E. López de Maturana, N. Malats, K. P. Olive, R. Rabadan, Pervasiveness of HLA allele-specific expression loss across tumor types. *Genome Med.* 15, 8 (2023).
19. A. Ladányi, B. Hegyi, T. Balatoni, G. Liszkay, R. Rohregger, C. Waldnig, J. Dudás, S. Ferrone, HLA Class I Downregulation in Progressing Metastases of Melanoma Patients Treated With Ipilimumab. *Pathol. Oncol. Res. POR* 28, 1610297 (2022).
20. S. Garcia-Recio, T. Hinoue, G. L. Wheeler, B. J. Kelly, A. C. Garrido-Castro, T. Pascual, A. A. De Cubas, Y. Xia, B. M. Felsheim, M. B. McClure, A. Rajkovic, E. Karaesmen, M. A. Smith, C. Fan, P. I. G. Ericsson, M. E. Sanders, C. J. Creighton, J. Bowen, K. Leraas, R. T. Burns, S. Coppens, A. Wheless, S. Rezk, A. L. Garrett, J. S. Parker, K. K. Foy, H. Shen, B. H. Park, I. Krop, C. Anders, J. Gastier-Foster, M. F. Rimawi, R. Nanda, N. U. Lin, C. Isaacs, P. K. Marcom, A. M. Storniolo, F. J. Couch, U. Chandran, M. Davis, J. Silverstein, A. Ropelewski, M. C. Liu, S. G. Hilsenbeck, L. Norton, A. L. Richardson, W. F. Symmans, A. C. Wolff, N. E. Davidson, L. A. Carey, A. V. Lee, J. M. Balko, K. A. Hoadley, P. W. Laird, E. R. Mardis, T. A. King, AURORA US Network, C. M. Perou, Multiomics in primary and metastatic breast tumors from the AURORA US network finds microenvironment and epigenetic drivers of metastasis. *Nat. Cancer* 4, 128–147 (2023).
21. A. López-Soto, L. Huergo-Zapico, J. A. Galván, L. Rodrigo, A. G. de Herreros, A. Astudillo, S. Gonzalez, Epithelial-mesenchymal transition induces an antitumor immune response mediated by NKG2D receptor. *J. Immunol. Baltim. Md 1950* 190, 4408–4419 (2013).
22. M. Villalba, M. G. Rathore, N. Lopez-Royuela, E. Krzywinska, J. Garaude, N. Allende-Vega, From tumor cell metabolism to tumor immune escape. *Int. J. Biochem. Cell Biol.* 45, 106–113 (2013).

23. S. Charni, J. I. Aguilo, J. Garaude, G. de Bettignies, C. Jacquet, R. A. Hipskind, D. Singer, A. Anel, M. Villalba, ERK5 knockdown generates mouse leukemia cells with low MHC class I levels that activate NK cells and block tumorigenesis. *J. Immunol. Baltim. Md 1950* 182, 3398–3405 (2009).
24. S. Charni, G. de Bettignies, M. G. Rathore, J. I. Aguiló, P. J. van den Elsen, D. Haouzi, R. A. Hipskind, J. A. Enriquez, M. Sanchez-Beato, J. Pardo, A. Anel, M. Villalba, Oxidative phosphorylation induces de novo expression of the MHC class I in tumor cells through the ERK5 pathway. *J. Immunol. Baltim. Md 1950* 185, 3498–3503 (2010).
25. E. Catalán, S. Charni, P. Jaime, J. I. Aguiló, J. A. Enríquez, J. Naval, J. Pardo, M. Villalba, A. Anel, MHC-I modulation due to changes in tumor cell metabolism regulates tumor sensitivity to CTL and NK cells. *Oncoimmunology* 4, e985924 (2015).
26. S. Belkahla, J. M. Brualla, A. Fayd'herbe de Maudave, P. Falvo, N. Allende-Vega, M. Constantinides, A. U. H. Khan, L. Coenon, C. Alexia, G. Mitola, P. Massa, S. Orecchioni, F. Bertolini, W. Mnif, J. Hernandez, A. Anel, M. Villalba, The metabolism of cells regulates their sensitivity to NK cells depending on p53 status. *Sci. Rep.* 12, 3234 (2022).
27. N. Allende-Vega, J. Marco Brualla, P. Falvo, C. Alexia, M. Constantinides, A. Fayd'herbe de Maudave, L. Coenon, D. Gitenay, G. Mitola, P. Massa, S. Orecchioni, F. Bertolini, I. Marzo, A. Anel, M. Villalba, Metformin sensitizes leukemic cells to cytotoxic lymphocytes by increasing expression of intercellular adhesion molecule-1 (ICAM-1). *Sci. Rep.* 12, 1341 (2022).
28. D. F. Barber, M. Faure, E. O. Long, LFA-1 contributes an early signal for NK cell cytotoxicity. *J. Immunol. Baltim. Md 1950* 173, 3653–3659 (2004).
29. T. Tataranni, C. Piccoli, Dichloroacetate (DCA) and Cancer: An Overview towards Clinical Applications. *Oxid. Med. Cell. Longev.* 2019, 8201079 (2019).
30. S. Kankotia, P. W. Stacpoole, Dichloroacetate and cancer: new home for an orphan drug? *Biochim. Biophys. Acta* 1846, 617–629 (2014).
31. A. U. H. Khan, N. Allende-Vega, D. Gitenay, S. Gerbal-Chaloin, C. Gondeau, D. N. Vo, S. Belkahla, S. Orecchioni, G. Talarico, F. Bertolini, M. Bozic, J. M. Valdivielso, F. Bejjani, I. Jariel, I. C. Lopez-Mejia, L. Fajas, C. H. Lecellier, J. Hernandez, M. Daujat, M. Villalba, The PDK1 Inhibitor Dichloroacetate Controls Cholesterol Homeostasis Through the ERK5/MEF2 Pathway. *Sci Rep* 7, 10654 (2017).
32. A. U. H. Khan, H. Salehi, C. Alexia, J. M. Valdivielso, M. Bozic, I. C. Lopez-Mejia, L. Fajas, S. Gerbal-Chaloin, M. Daujat-Chavanieu, D. Gitenay, M. Villalba, Glucose Starvation or Pyruvate Dehydrogenase Activation Induce a Broad, ERK5-Mediated, Metabolic Remodeling Leading to Fatty Acid Oxidation. *Cells* 11, 1392 (2022).
33. B. Stecca, E. Rovida, Impact of ERK5 on the Hallmarks of Cancer. *Int. J. Mol. Sci.* 20, 1426 (2019).
34. W. Jiang, F. Cai, H. Xu, Y. Lu, J. Chen, J. Liu, N. Cao, X. Zhang, X. Chen, Q. Huang, H. Zhuang, Z.-C. Hua, Extracellular signal regulated kinase 5 promotes cell migration, invasion and lung metastasis in a FAK-dependent manner. *Protein Cell* 11, 825–845 (2020).
35. S. Pavan, N. Meyer-Schaller, M. Diepenbruck, R. K. R. Kalathur, M. Saxena, G. Christofori, A kinome-wide high-content siRNA screen identifies MEK5-ERK5 signaling as critical for breast cancer cell

EMT and metastasis. *Oncogene* 37, 4197–4213 (2018).

36. M. Villalba, D. Gitenay, S. Zemiti, J.-F. Rossi, M. Campos-Mora, Is the MAPK ERK5 the nexus from FAO to NK cell-mediated metastasis immune surveillance? *Front. Immunol.* 16, 1641865 (2025).
37. C. Corbet, E. Bastien, J. P. Santiago de Jesus, E. Dierge, R. Martherus, C. Vander Linden, B. Doix, C. Degavre, C. Guilbaud, L. Petit, C. Michiels, C. Dessy, Y. Larondelle, O. Feron, TGFβ2-induced formation of lipid droplets supports acidosis-driven EMT and the metastatic spreading of cancer cells. *Nat. Commun.* 11, 454 (2020).
38. A. Amaro, G. Angelini, V. Mirisola, A. I. Esposito, D. Reverberi, S. Matis, M. Maffei, W. Giaretti, M. Viale, R. Gangemi, L. Emionite, S. Astigiano, M. Cilli, B. E. Bachmeier, P. H. Killian, A. Albini, U. Pfeffer, A highly invasive subpopulation of MDA-MB-231 breast cancer cells shows accelerated growth, differential chemoresistance, features of apocrine tumors and reduced tumorigenicity in vivo. *Oncotarget* 7, 68803–68820 (2016).
39. W. Budzynski, C. Radzikowski, Cytotoxic cells in immunodeficient athymic mice. *Immunopharmacol. Immunotoxicol.* 16, 319–346 (1994).
40. E. D. Michelakis, G. Sutendra, P. Dromparis, L. Webster, A. Haromy, E. Niven, C. Maguire, T.-L. Gammer, J. R. Mackey, D. Fulton, B. Abdulkarim, M. S. McMurtry, K. C. Petruk, Metabolic modulation of glioblastoma with dichloroacetate. *Sci. Transl. Med.* 2, 31ra34 (2010).
41. S. Belkahla, J. M. Brualla, A. Fayd'herbe de Maudave, P. Falvo, N. Allende-Vega, M. Constantinides, A. U. H. Khan, L. Coenon, C. Alexia, G. Mitola, P. Massa, S. Orecchioni, F. Bertolini, W. Mnif, J. Hernandez, A. Anel, M. Villalba, The metabolism of cells regulates their sensitivity to NK cells depending on p53 status. *Sci. Rep.* 12, 3234 (2022).
42. N. Allende-Vega, M. Villalba, Metabolic stress controls mutant p53 R248Q stability in acute myeloid leukemia cells. *Sci. Rep.* 9, 5637 (2019).
43. N. Allende-Vega, E. Krzywinska, S. Orecchioni, N. Lopez-Royuela, F. Reggiani, G. Talarico, J. F. Rossi, R. Rossignol, Y. Hicheri, G. Cartron, F. Bertolini, M. Villalba, The presence of wild type p53 in hematological cancers improves the efficacy of combinational therapy targeting metabolism. *Oncotarget* 6, 19228–19245 (2015).
44. Y. Teng, X. Xie, S. Walker, D. T. White, J. S. Mumm, J. K. Cowell, Evaluating human cancer cell metastasis in zebrafish. *BMC Cancer* 13, 453 (2013).
45. M. Ito, H. Hiramatsu, K. Kobayashi, K. Suzue, M. Kawahata, K. Hioki, Y. Ueyama, Y. Koyanagi, K. Sugamura, K. Tsuji, T. Heike, T. Nakahata, NOD/SCID/gamma(c)(null) mouse: an excellent recipient mouse model for engraftment of human cells. *Blood* 100, 3175–3182 (2002).
46. L. D. Shultz, B. L. Lyons, L. M. Burzenski, B. Gott, X. Chen, S. Chaleff, M. Kotb, S. D. Gillies, M. King, J. Mangada, D. L. Greiner, R. Handgretinger, Human lymphoid and myeloid cell development in NOD/LtSz-scid IL2R gamma null mice engrafted with mobilized human hemopoietic stem cells. *J. Immunol. Baltim. Md 1950* 174, 6477–6489 (2005).
47. E. Jarc, T. Petan, Lipid Droplets and the Management of Cellular Stress. *Yale J. Biol. Med.* 92, 435–452 (2019).

48. T. Petan, E. Jarc, M. Jusović, Lipid Droplets in Cancer: Guardians of Fat in a Stressful World. *Mol. Basel Switz.* 23, 1941 (2018).
49. E. Jarc, T. Petan, A twist of FATe: Lipid droplets and inflammatory lipid mediators. *Biochimie* 169, 69–87 (2020).
50. K. Bensaad, E. Favaro, C. A. Lewis, B. Peck, S. Lord, J. M. Collins, K. E. Pinnick, S. Wigfield, F. M. Buffa, J.-L. Li, Q. Zhang, M. J. O. Wakelam, F. Karpe, A. Schulze, A. L. Harris, Fatty acid uptake and lipid storage induced by HIF-1α contribute to cell growth and survival after hypoxia-reoxygenation. *Cell Rep.* 9, 349–365 (2014).
51. M. T. Accioly, P. Pacheco, C. M. Maya-Monteiro, N. Carrossini, B. K. Robbs, S. S. Oliveira, C. Kaufmann, J. A. Morgado-Diaz, P. T. Bozza, J. P. B. Viola, Lipid bodies are reservoirs of cyclooxygenase-2 and sites of prostaglandin-E2 synthesis in colon cancer cells. *Cancer Res.* 68, 1732–1740 (2008).
52. E. D. Michelakis, L. Webster, J. R. Mackey, Dichloroacetate (DCA) as a potential metabolic-targeting therapy for cancer. *Br. J. Cancer* 99, 989–994 (2008).
53. R. Camarda, A. Y. Zhou, R. A. Kohnz, S. Balakrishnan, C. Mahieu, B. Anderton, H. Eyob, S. Kajimura, A. Tward, G. Krings, D. K. Nomura, A. Goga, Inhibition of fatty acid oxidation as a therapy for MYC-overexpressing triple-negative breast cancer. *Nat. Med.* 22, 427–432 (2016).
54. L. Tirinato, F. Pagliari, T. Limongi, M. Marini, A. Falqui, J. Seco, P. Candeloro, C. Liberale, E. Di Fabrizio, An Overview of Lipid Droplets in Cancer and Cancer Stem Cells. *Stem Cells Int.* 2017, 1656053 (2017).
55. S. Hu, Z. Li, J. Cores, K. Huang, T. Su, P.-U. Dinh, K. Cheng, Needle-Free Injection of Exosomes Derived from Human Dermal Fibroblast Spheroids Ameliorates Skin Photoaging. *ACS Nano* 13, 11273–11282 (2019).
56. O. Melaiu, V. Lucarini, L. Cifaldi, D. Fruci, Influence of the Tumor Microenvironment on NK Cell Function in Solid Tumors. *Front. Immunol.* 10, 3038 (2019).
57. L. Gorvel, D. Olive, Targeting the “PVR-TIGIT axis” with immune checkpoint therapies. *F1000Research* 9, F1000 Faculty Rev-354 (2020).
58. K. E. Sloan, B. K. Eustace, J. K. Stewart, C. Zehetmeier, C. Torella, M. Simeone, J. E. Roy, C. Unger, D. N. Louis, L. L. Ilag, D. G. Jay, CD155/PVR plays a key role in cell motility during tumor cell invasion and migration. *BMC Cancer* 4, 73 (2004).
59. D. Pende, C. Bottino, R. Castriconi, C. Cantoni, S. Marcenaro, P. Rivera, G. M. Spaggiari, A. Dondero, B. Carnemolla, N. Reymond, M. C. Mingari, M. Lopez, L. Moretta, A. Moretta, PVR (CD155) and Nectin-2 (CD112) as ligands of the human DNAM-1 (CD226) activating receptor: involvement in tumor cell lysis. *Mol. Immunol.* 42, 463–469 (2005).
60. P. Kučan Brlić, T. Lenac Roviš, G. Cinamon, P. Tsukerman, O. Mandelboim, S. Jonjić, Targeting PVR (CD155) and its receptors in anti-tumor therapy. *Cell. Mol. Immunol.* 16, 40–52 (2019).
61. O. Kuda, M. Brezinova, J. Silhavy, V. Landa, V. Zidek, C. Dodia, F. Kreuchwig, M. Vrbacky, L. Balas, T. Durand, N. Hübner, A. B. Fisher, J. Kopecky, M. Pravenec, Nrf2-Mediated Antioxidant Defense and

Peroxiredoxin 6 Are Linked to Biosynthesis of Palmitic Acid Ester of 9-Hydroxystearic Acid. *Diabetes* 67, 1190–1199 (2018).

62. E. Vivier, E. Tomasello, M. Baratin, T. Walzer, S. Ugolini, Functions of natural killer cells. *Nat. Immunol.* 9, 503–510 (2008).
63. M. Villalba, C. Alexia, A. Bellin-Robert, A. Fayd'herbe de Maudave, D. Gitenay, Non-Genetically Improving the Natural Cytotoxicity of Natural Killer (NK) Cells. *Front. Immunol.* 10, 3026 (2019).
64. S. F. Powell, M. Mazurczak, E. G. Dib, J. S. Bleeker, L. H. Geeraerts, M. Tinguely, M. M. Lohr, S. C. McGraw, A. W. Jensen, C. A. Ellison, L. J. Black, S. E. Puumala, V. J. Reed, W. K. Miskimins, J. H. Lee, W. C. Spanos, Phase II study of dichloroacetate, an inhibitor of pyruvate dehydrogenase, in combination with chemoradiotherapy for unresected, locally advanced head and neck squamous cell carcinoma. *Invest. New Drugs* 40, 622–633 (2022).
65. M. S. Hasim, M. Marotel, J. J. Hodgins, E. Vulpis, O. J. Makinson, S. Asif, H.-Y. Shih, A. K. Scheer, O. MacMillan, F. G. Alonso, K. P. Burke, D. P. Cook, R. Li, M. T. Petrucci, A. Santoni, P. G. Fallon, A. H. Sharpe, G. Sciumè, A. Veillette, A. Zingoni, D. A. Gray, A. McCurdy, M. Ardolino, When killers become thieves: Trogocytosed PD-1 inhibits NK cells in cancer. *Sci. Adv.* 8, eabj3286 (2022).
66. M. Campos-Mora, W. Jacot, G. Garcin, M.-L. Depondt, M. Constantinides, C. Alexia, M. Villalba, NK cells in peripheral blood carry trogocytosed tumor antigens from solid cancer cells. *Front. Immunol.* 14, 1199594 (2023).
67. S. Bonnet, S. L. Archer, J. Allalunis-Turner, A. Haromy, C. Beaulieu, R. Thompson, C. T. Lee, G. D. Lopaschuk, L. Puttagunta, S. Bonnet, G. Harry, K. Hashimoto, C. J. Porter, M. A. Andrade, B. Thebaud, E. D. Michelakis, A mitochondria-K+ channel axis is suppressed in cancer and its normalization promotes apoptosis and inhibits cancer growth. *Cancer Cell* 11, 37–51 (2007).
68. W. Jiang, F. Cai, H. Xu, Y. Lu, J. Chen, J. Liu, N. Cao, X. Zhang, X. Chen, Q. Huang, H. Zhuang, Z.-C. Hua, Extracellular signal regulated kinase 5 promotes cell migration, invasion and lung metastasis in a FAK-dependent manner. *Protein Cell* 11, 825–845 (2020).
69. M. Rios Garcia, B. Steinbauer, K. Srivastava, M. Singhal, F. Mattijssen, A. Maida, S. Christian, H. Hess-Stumpp, H. G. Augustin, K. Müller-Decker, P. P. Nawroth, S. Herzig, M. Berriel Diaz, Acetyl-CoA Carboxylase 1-Dependent Protein Acetylation Controls Breast Cancer Metastasis and Recurrence. *Cell Metab.* 26, 842–855.e5 (2017).
70. T. Farge, J. Nakhle, D. Lagarde, G. Cognet, N. Polley, R. Castellano, M.-L. Nicolau, C. Bosc, M. Sabatier, A. Sahal, E. Saland, Y. Jeanson, N. Guiraud, E. Boet, C. Bergoglio, M. Gotanègre, P.-L. Mouchel, L. Stuani, C. Larrue, M. Sallese, V. De Mas, C. Moro, C. Dray, Y. Collette, I. Raymond-Letron, I. Ader, C. Récher, J.-E. Sarry, F. Cabon, F. Vergez, A. Carrière, CD36 Drives Metastasis and Relapse in Acute Myeloid Leukemia. *Cancer Res.* 83, 2824–2838 (2023).
71. J. S. Hale, B. Otvos, M. Sinyuk, A. G. Alvarado, M. Hitomi, K. Stoltz, Q. Wu, W. Flavahan, B. Levison, M. L. Johansen, D. Schmitt, J. M. Neltner, P. Huang, B. Ren, A. E. Sloan, R. L. Silverstein, C. L. Gladson, J. A. DiDonato, J. M. Brown, T. McIntyre, S. L. Hazen, C. Horbinski, J. N. Rich, J. D. Lathia, Cancer stem

cell-specific scavenger receptor CD36 drives glioblastoma progression. *Stem Cells Dayt. Ohio* 32, 1746–1758 (2014).

72. S. Belkahla, J. M. Brualla, A. Fayd'herbe de Maudave, P. Falvo, N. Allende-Vega, M. Constantinides, A. U. H. Khan, L. Coenon, C. Alexia, G. Mitola, P. Massa, S. Orecchioni, F. Bertolini, W. Mnif, J. Hernandez, A. Anel, M. Villalba, The metabolism of cells regulates their sensitivity to NK cells depending on p53 status. *Sci. Rep.* 12, 3234 (2022).
73. D. Sanchez-Martinez, N. Allende-Vega, S. Orecchioni, G. Talarico, A. Cornillon, D. N. Vo, C. Rene, z-y Lu, E. Krzywinska, A. Anel, E. M. Galvez, J. Pardo, B. Robert, P. Martineau, Y. Hicheri, F. Bertolini, G. Cartron, M. Villalba, Expansion Of Allogeneic NK Cells With Efficient Antibody-Dependent Cell Cytotoxicity Against Multiple Tumor Cells. *Theranostic* 8, 3856–3869 (2018).
74. C. Reina-Ortiz, M. Constantinides, A. Fayd-Herbe-de-Maudave, J. Présumey, J. Hernandez, G. Cartron, D. Giraldos, R. Díez, I. Izquierdo, G. Azaceta, L. Palomera, I. Marzo, J. Naval, A. Anel, M. Villalba, Expanded NK cells from umbilical cord blood and adult peripheral blood combined with daratumumab are effective against tumor cells from multiple myeloma patients. *Oncoimmunology* 10, 1853314 (2020).
75. C. Goertzen, D. Eymael, M. Magalhaes, Three-Dimensional Quantification of Spheroid Degradation-Dependent Invasion and Invadopodia Formation. *Biol. Proced. Online* 20, 20 (2018).
76. J. Nakayama, H. Makinoshima, Zebrafish-Based Screening Models for the Identification of Anti-Metastatic Drugs. *Mol. Basel Switz.* 25, 2407 (2020).
77. L. Coënon, E. Rigal, H. Courot, C. Multrier, S. Zemiti, J. Lambour, M. Pugnière, M. de Toledo, G. Bossis, G. Cartron, B. Robert, P. Martineau, B. Fauvel, J. Presumey, M. Villalba, Generation of non-genetically modified, CAR-like, NK cells. *J. Immunother. Cancer* 12, e009070 (2024).

Figures

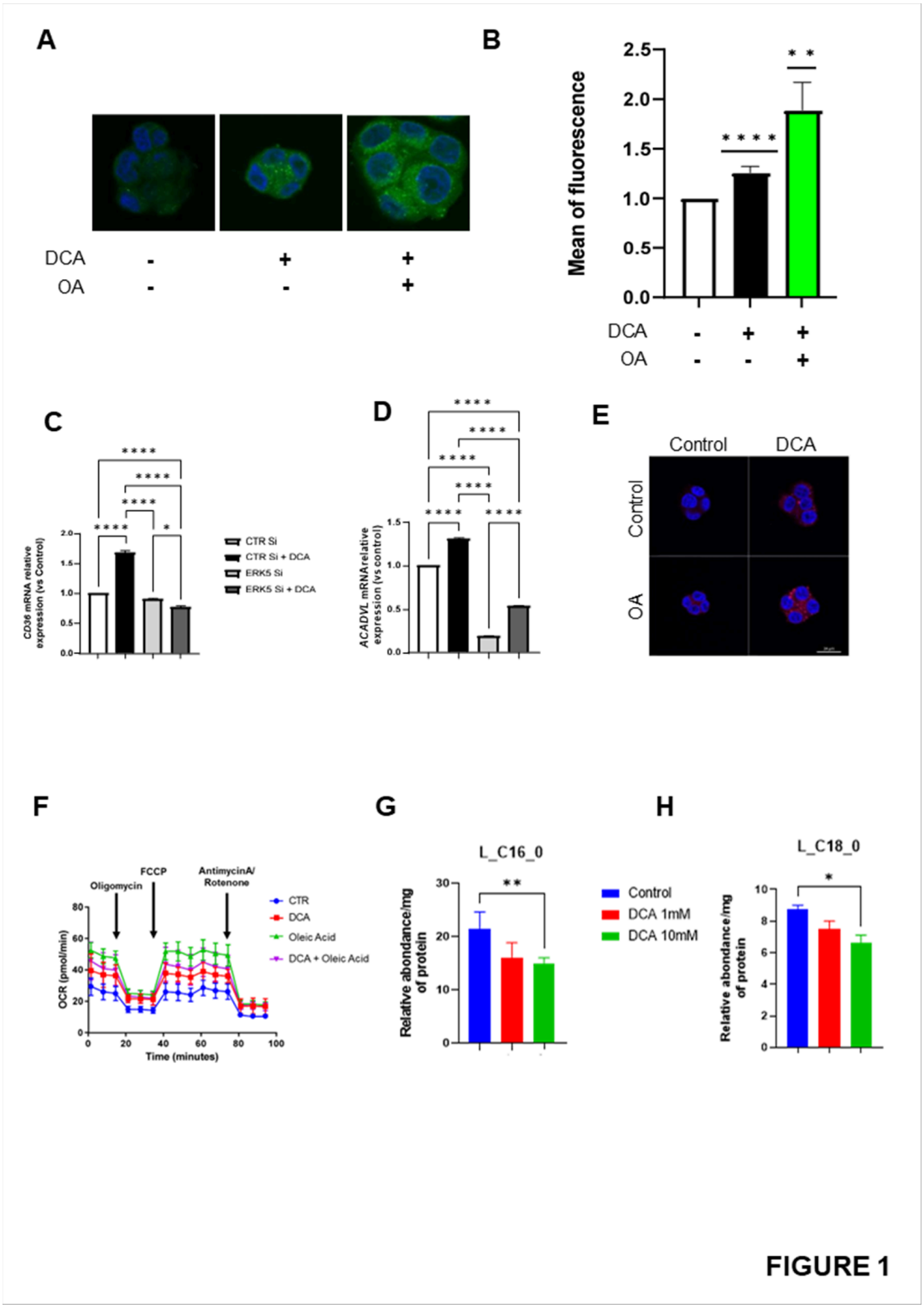


Figure 1

DCA increases lipid metabolism and oxidative phosphorylation (OXPHOS) in HCT116 cells. A-B) HCT116 cells were treated with 5mM DCA and 3μM oleic acid (OA) for 48h. Cells were incubated with Bodipy and DAPI and analyzed by immunofluorescence (A) or by flow cytometry (B) in 3 independent experiments. C-D) Cells were transfected with a siRNA control (siControl) or with a siRNA for ERK5 (siERK5). Forty-eight hours after transfection 200000 cells/well were seeded in 6 wells plates and

treated with 10mM DCA. After 48h, RNA was extracted and the relative mRNA level of *CD36* (C) and *ACADVL CD36* (D) were assessed and normalized to *β-actin* mRNA (n=3). E) Cells were treated with 5mM DCA and/or 3µM OA. After 48h, CD36 expression (in red) was assessed by microscopy (n=3). F) Cells were treated as in (A) and the oxygen consumption rate (OCR) was analyzed in a Seahorse. Statistical analysis was performed using one-way Anova followed by a Tukey multiple comparison test. G-H) HCT116 cells were treated with 1 and 10mM of DCA and analyzed by mass spectrometry. Graphs represent mean +/- SD. ** p < 0.05, ** p < 0.01, *** p < 0.001, **** p < 0.0001*; Tukey's test was used to compare condition to control or as depicted in the graphic.

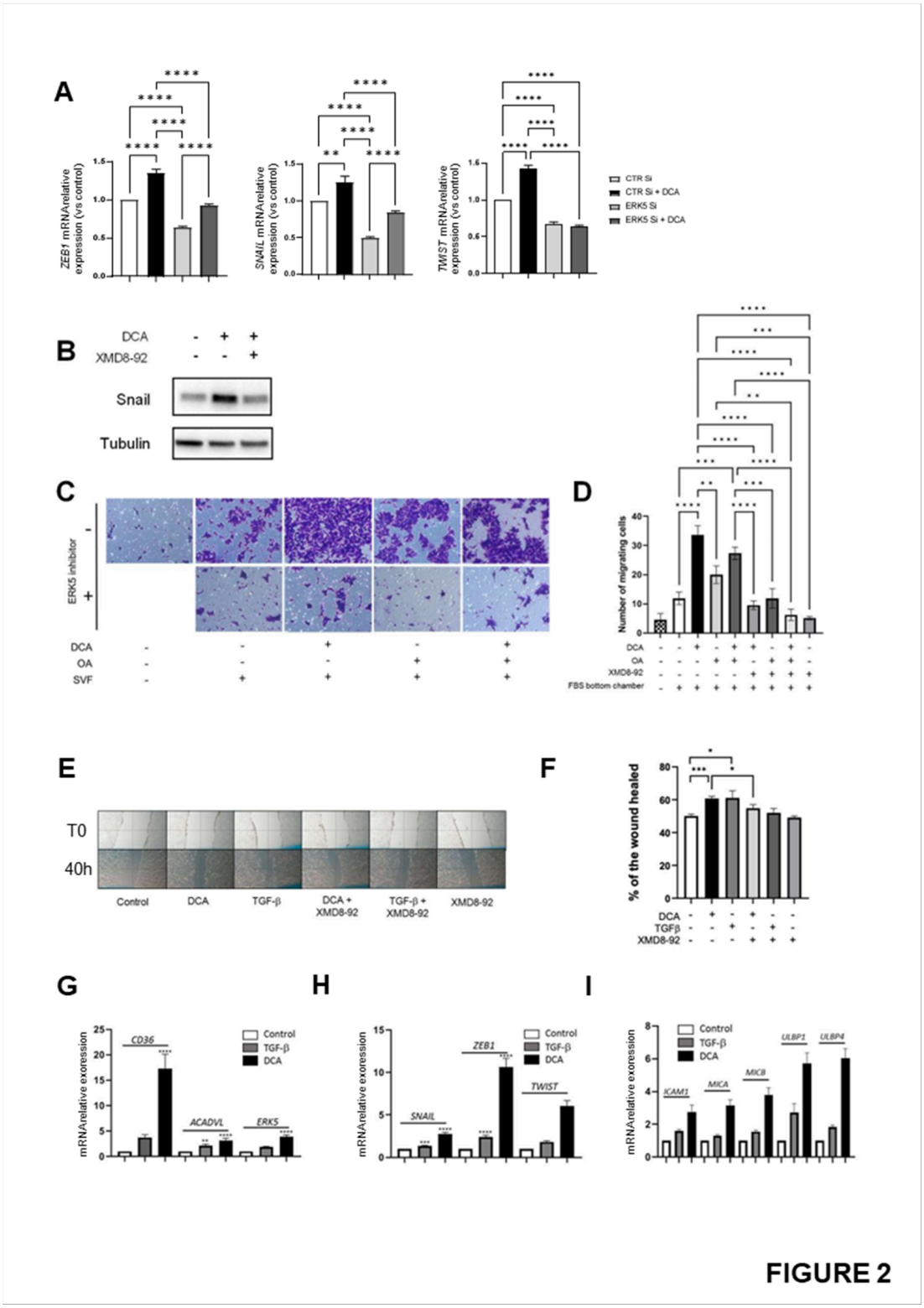


Figure 2

FAO induces EMT and a migratory phenotype in 2-Dimension (2D) through the ERK5 pathway. A) Twenty-four hours after seeding and at 60% confluency, HCT116 cells were transfected with either siControl or siERK5 and 48h later treated with 10mM DCA. After 48h, RNA was extracted and the relative mRNA level of *ZEB1*, *SNAIL* and *TWIST* were assessed and normalized to *β-actin* mRNA levels (n=3). B) Cells were seeded and treated for 48h with 20mM DCA and 5 µM of the ERK5 inhibitor XMD8-92. SNAIL

and tubulin expression were analyzed by western blot. C) 7500 HCT116 cells were seeded in inserts of a transwell system in a FBS-deprived medium and incubated with 10mM DCA, 3µM OA and/or 5µM of XMD8-92. The lower part of the transwell contained 10% FBS to attract cells. After 48h we analyzed the number of colonies formed on the other side of the insert after fixation and crystal violet staining (representative of 3 experiments). D) Three fields of the 3 independent experiments were analyzed by counting the number of colonies. E) Four million HCT116 cells were seeded per well and one day later a wound was created by scratching the cell layer vertically with a 100µL tip. Pictures were taken at this initial time, then cells were treated the same day and each day with 10mM DCA, 2ng/mL TGFβ-2 and/or 5µM of XMD8-92. Representative images of the wound healing at initial time and after 40h are shown. F) The area of the wounds of 3 independent experiments were calculated per condition with the software "ImageJ". G-I) HCT116 cells were seeded at $2x10^5$ cells per well in 6 wells plates and treated for 24h with 10mM DCA or 2ng/mL TGFβ-2. RNA was extracted and mRNA gene levels quantified. These were split in metabolic genes (G; *CD36, ACDVL and ERK5*), EMT-related genes (H; *SNAIL, ZEB1, TWIST*) and NK cell ligands (I; *MICA, MICB, ULBP1 and ULBP4*). The data were analyzed with the 2^ (-DDCt) method and normalized to *β-actin* mRNA levels. The graphs represent mean+/-SD of the relative mRNA (n=3). * $p < 0.05$, ** $p < 0.01$, *** $p < 0.001$, **** $p < 0.0001$; Tukey's test was used to compare condition to control or as depicted in the graphic.

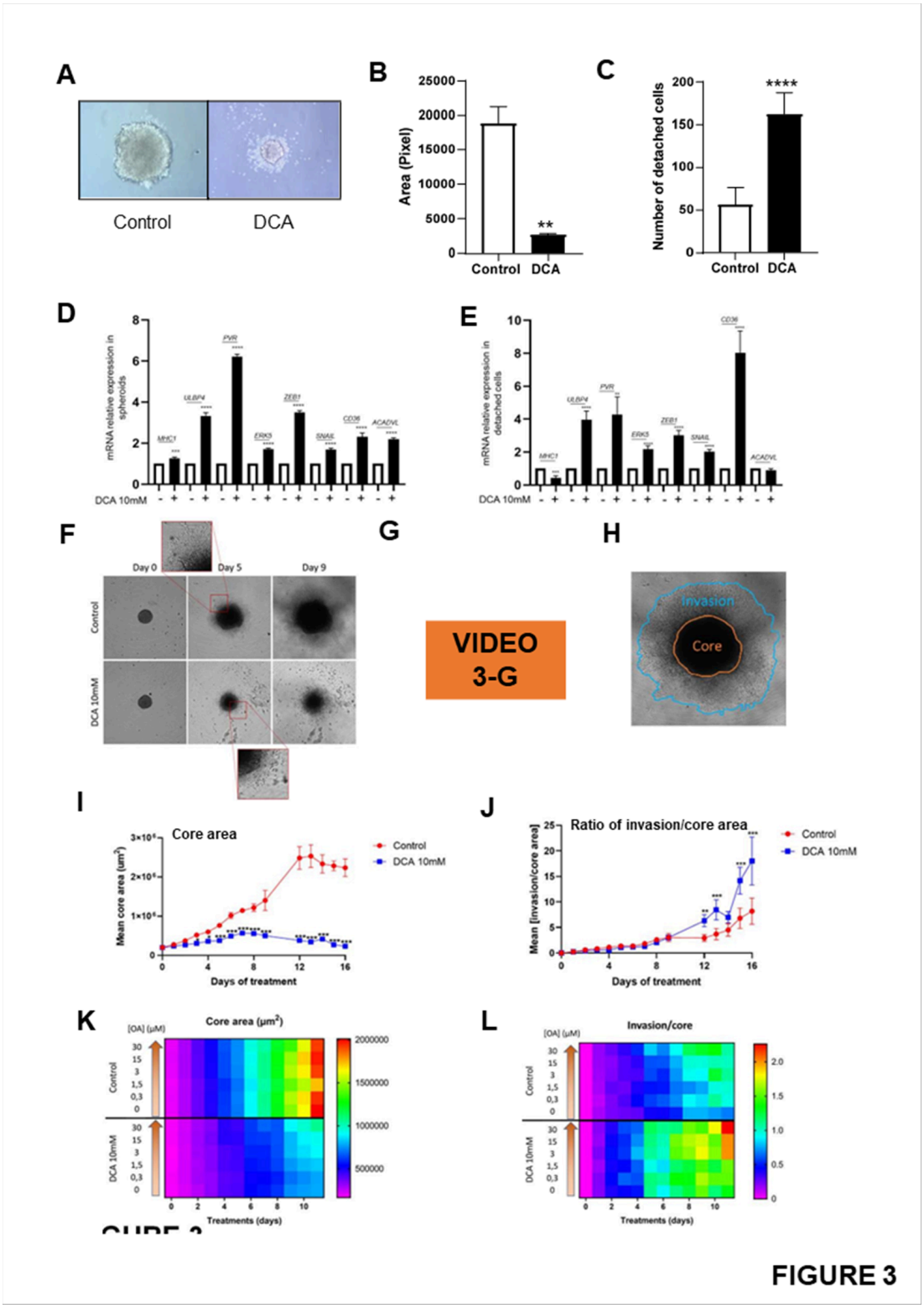


Figure 3

DCA decreases tumor growth and increases tumor cell detachment and invasion in *in vitro* 3D models. A-D) HCT116 were grown to generate spheroids in “Ultra Low attachment plates” in DMEM F12 B27 + Insulin/EGF/FGF medium and treated with 10mM DCA for 7 days. Images A) were taken, B) the area of the spheres and C) the number of cells detached from them were analyzed with the software "ImageJ". The graphs represent the mean +/- SD. D-E) Spheroids were individually collected from the wells and

pooled. The remaining detached cells were also pooled for each condition. 96 wells were pooled for each condition to obtain enough RNA, which was extracted and RT-QPCR performed for each condition: spheres (D) and detached cells (E). The data were analyzed with the 2^ (-DDCt) method and normalized to *β-actin* mRNA levels. The graphs represent mean+/-SD of the relative mRNA (n=3). * $p < 0.05$, ** $p < 0.01$, *** $p < 0.001$, **** $p < 0.0001$; Tukey's test was used to compare condition to control or as depicted in the graphic. F-L) HCT116 cells were cultivated in ultra-low attachment 96-well plate. When spheroids were formed, they were transferred in U-bottom 96-well plate and resuspended in GeltrexTM. Treatments were performed every day from day 0 and during 16 days and images were taken on a Cytation 5. F) Representative pictures of spheroids growth and tumor invasive profile in GeltrexTM. G) Video of cell invasion at different time points, with DCA-treated cells at right of the images. H) Schematic representation of the sphere (the core) and the invasive area (in blue) generated by the cells around the sphere. I) Growth curve of the spheroids' core. J) Invasiveness is measured by the ratio between the invasion area and the core area. K-L) Heat maps of the core (K) or the invasion area (L) of spheroids growing with or without 10mM DCA in the presence of different concentrations of OA. We analyzed 6 wells per condition and the experiment were replicated 3 times. All the results were treated by GraphPad Prism 9 software with multiple t test; statistical significance determined using the Holm-Sidak method; alpha = 0.05. * $p<0.05$; **$p<0.01$, ***$p<0.001$, ****$p<0.0001$. * $p<0.05$; **$p<0.01$, ***$p<0.001$, ****$p<0.0001$; unpaired T test.

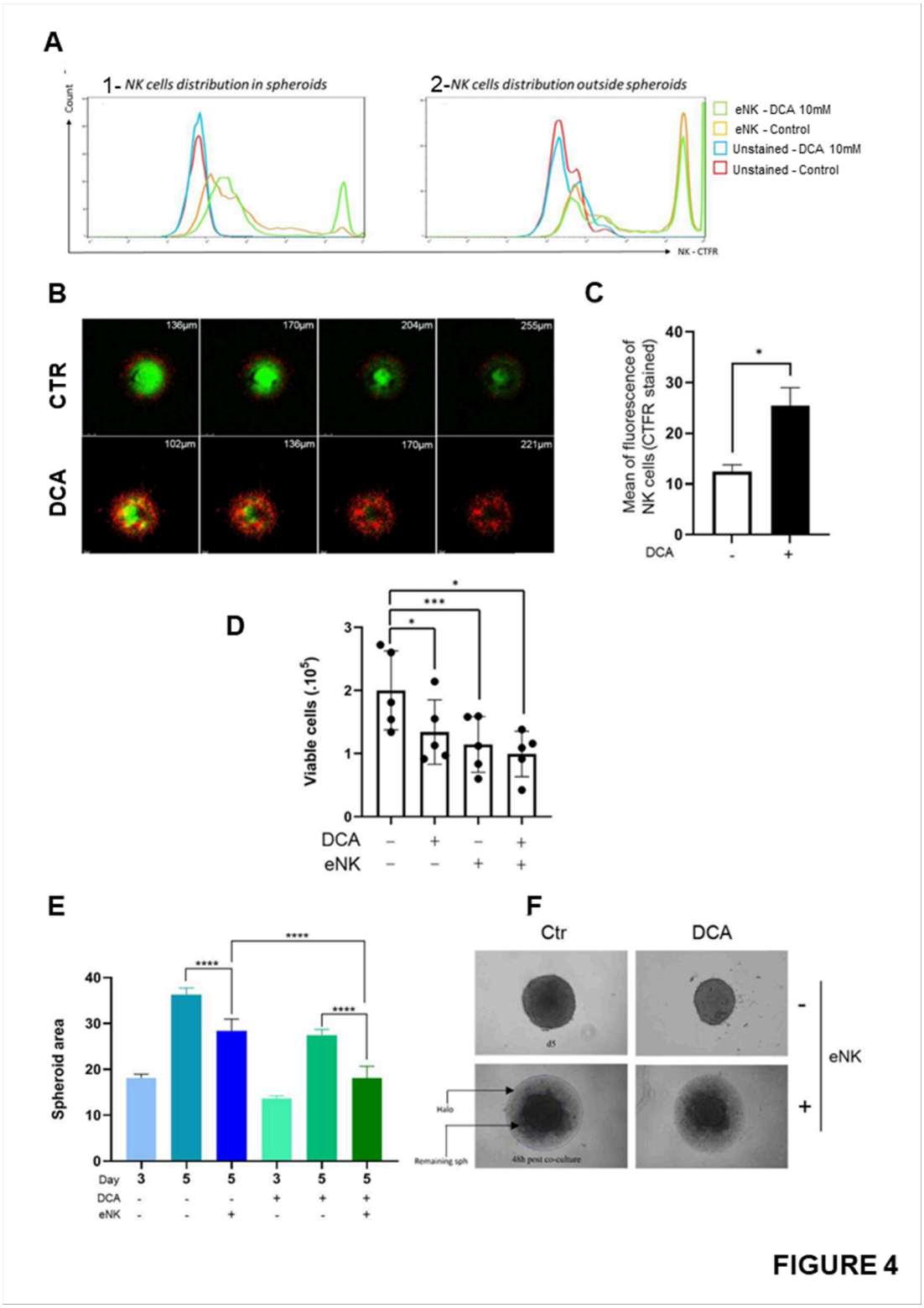


Figure 4

DCA increases NK cell infiltration into tumor cell spheroids and sensitizes tumor cells to NK cell-mediated killing. To assess eNK infiltration in spheroids both flow cytometry (FC) and confocal microscopy were used. A) FC: spheroids pre-treated with DCA or H2O (DCA vehicle) for 48 hours were cocultured with CTFR-stained eNK cells for 8 hours. We collected separately spheroids and the remaining cells in the media to compare the infiltrated and the media's remaining fraction of eNK cells.

Cell fluorescence was assessed: CTFR positive population in the right side of the graphs represents NK cells whereas spheroids tumor cells are the CTFR negative population. B) Confocal microscopy: Calcein-AM (green) stained spheroids and CTFR stained eNK cells (red) were co-cultured for 24h, and imaging was processed by confocal microscopy (Leica-SP8). Images represent different confocal planes of the spheroids. C) Fluorescence intensity was analyzed with the software "ImageJ”. The graphs represent the mean ± SD. D) Twenty thousand HCT116 cells were plated in 24-well plates and treated with 10mM DCA or H2O for 24h then incubated with eNK at an effector: target (E:T) ratio of 2:1. After 6 hours, HCT116 cells were counted. Graphs show mean ± SD of 5 independent eNK expansions. Statistical analysis was performed by the paired t test using the GraphPad Prism 9. E) After seeding, tumor spheroids were treated daily for 3 days with 10 mM DCA or H2O. eNK cells were added at E:T ratio of 2:1 for 48h. Cytotoxicity (spheroid destruction) was monitored by brightfield microscopy, and Fiji software measured and analyzed the solid spheroid area as described in (F). The graph represents the mean ± SD of the sphere area of 24 spheroids which were processed in 2 independent days, i.e. 12 spheroids/experiment. Statistical significance was analyzed by one-way ANOVA followed by Tukey’s multiple comparison test. * $p<0.05$; ** $p<0.01$, *** $p<0.001$, **** $p<0.0001$.

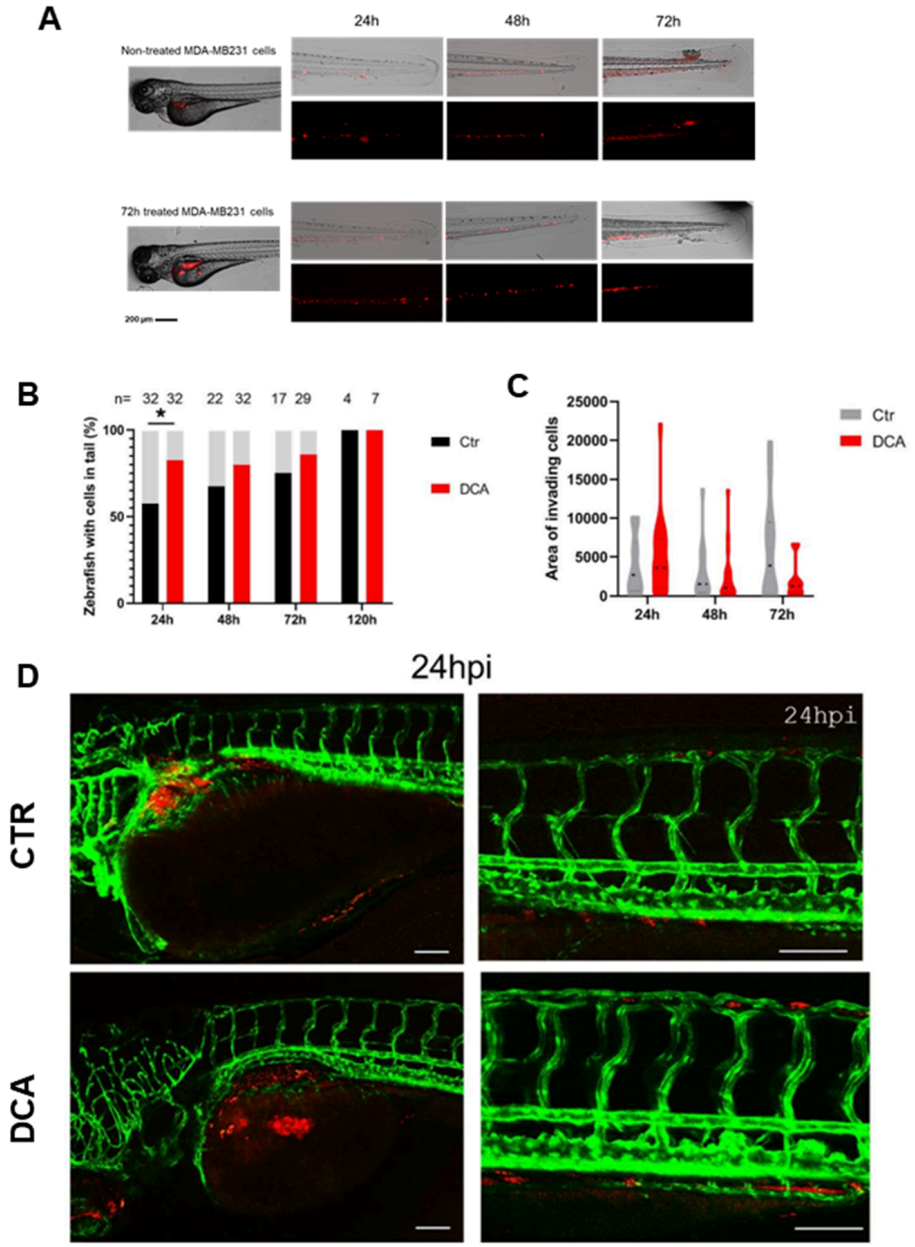


FIGURE 5

Figure 5

DCA induces invasion *in vivo*in a zebrafish model. A) In a zebrafish invasion assay, MDA-MB231 cells pretreated or not with 10mM DCA were labelled with CTFR and injected in the periyolk of 48hpf zebrafishes larvae. Epifluorescence images (inverted confocal microscope TCS SP5, Leica systems) were taken at 24, 48, 72 and 120h and cell migration was quantified. Scale bar represents 100 µm. B) The number of zebrafish with metastatic cells in the tail was counted at 24, 48, 72 and 120h post

engraftment. Statistical differences were analyzed using chi square test, * p<0.05. C) Graph depicts the area of invading cells in zebrafish with metastasis; n=3.

D) DCA enhances perivascular metastasis in the caudal part at 24h post injection (hpi). The same human cells were equally engrafted in transgenic zebrafish line: Tg(Kdrl:egfp to visualize the vascular system (green). High-resolution images were acquired using a confocal microscope. Scale bar=100µm.

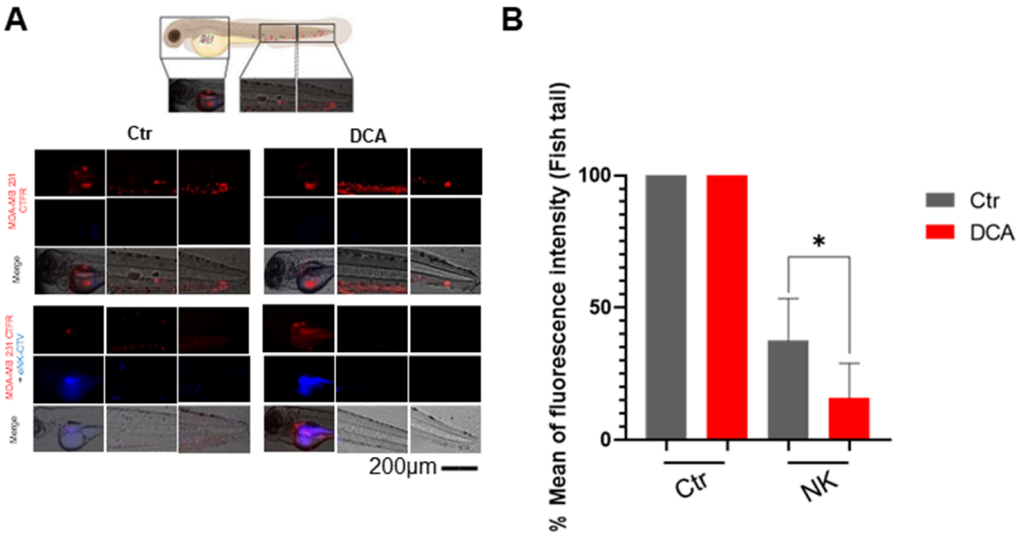


FIGURE 6

Figure 6

DCA-treated migratory cells are more susceptible to NK-cell-mediated control. A) Fluorescently/CTFR labelled MDA-MB-231 breast cancer cells (red), either untreated or DCA-treated, were co-injected together with eNK cells (blue) into the perivitelline space of 48 hpf zebrafish larvae at a 5:1 NK-to-cancer cell ratio. Pictures were taken 24 hours post-engraftment. **B)** Graph represents the mean ± SD of two independent experiments. Tumor cell migration was quantified by measuring the mean fluorescence intensity of labeled tumor cells in the tail region of zebrafish larvae. Fluorescence values were normalized to the corresponding tumor-only control conditions (set to 100%). Data represent the percentage of mean fluorescence intensity in the presence of NK cells relative to their respective controls. Data are represented as mean ± SD (n=10 per group). Statistical significance was assessed using a non-parametric Mann–Whitney test * $p<0.05$.

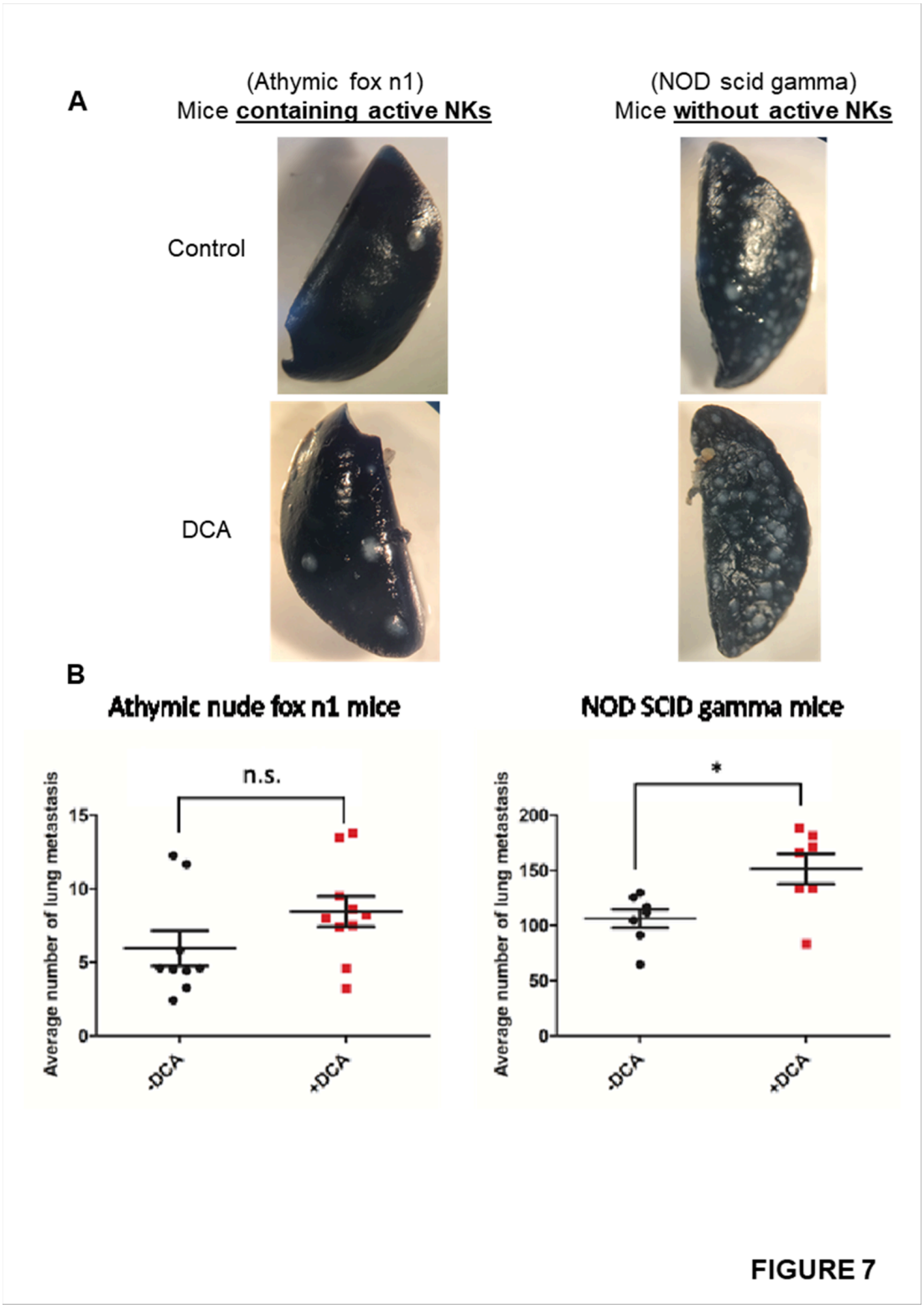


Figure 7

DCA-induced lung metastasis are controlled by NK cells. One million 4T1-luciferase breast cancer cells were engrafted into the fourth mammary fat pad of 7-week-old female athymic nude fox n1 mice (n=20) or NOD SCID-g mice (n=14) and were randomized into two groups receiving either DCA (100 mg/kg/day in water, oral gavage Monday–Friday) or vehicle alone, beginning the day after implantation and continuing for 17 days, during which body weight and tumor volume were measured every week. Mice

were weighed every 2 days and tumor volume was measured using a Caliper. After 3 weeks, mice were sacrificed by cervical dislocation and tumors were extracted and measured. A) Lungs were injected with a needle through the trachea with a solution of 15% Indian ink in distilled water, until the lungs were completely swollen. Black swollen lungs were then extracted from the mice and fixed using Fekete's solution (40 ml of glacial acetic acid, 80 ml of 37% Formalin, 580 ml of (100%) ethanol and 200 ml of water). B) Metastases in the lung were observed as white (non-colored) dots and the different lobes were dissociated to accurately count the number of metastases in each lobe. Data were evaluated using two-way ANOVA for longitudinal measurements and unpaired t-tests or Mann–Whitney tests for end point comparisons, with $p < 0.05$ considered significant.

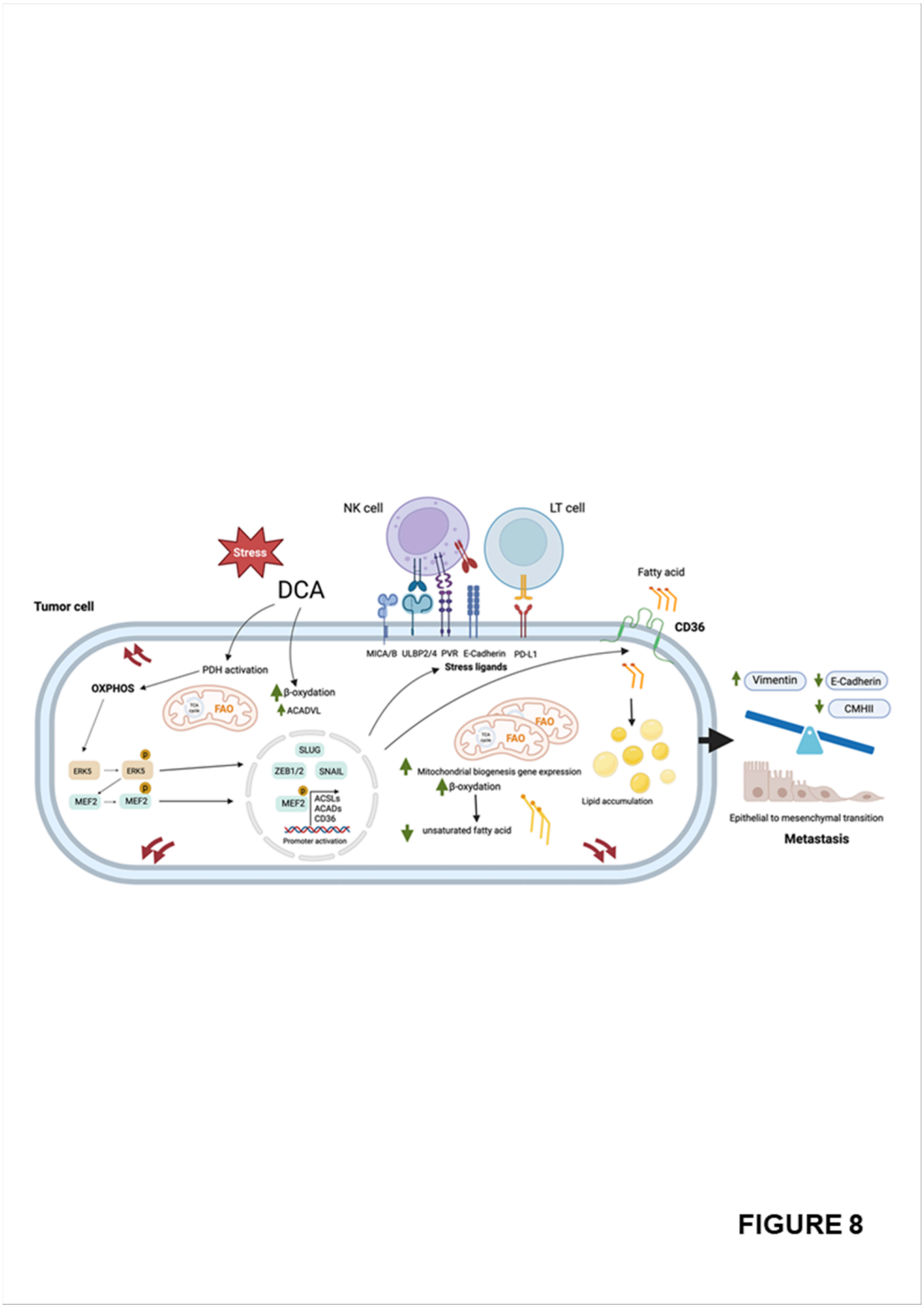


Figure 8

The relationship between lipid metabolism, metastasis, and NK cell-mediated tumor immune surveillance. The graphical abstract describes how forcing tumor cells to perform fatty acid oxidation (FAO) with dichloroacetate (DCA) activates the ERK5 pathway. This activation induces the expression of lipid metabolism proteins (such as CD36, ACSLs, and ACADs) that promote lipid accumulation in lipid droplets. Concurrently, DCA upregulates various transcription factors involved in the epithelial-to-

mesenchymal transition (EMT), including ZEB1/2, SLUG, and SNAIL, thereby facilitating a metastatic phenotype. These changes in metastatic cells promote the expression of stress ligands (e.g., MICA/B, ULBP2, and PVR), enhancing NK cell recognition via the activating receptors NKG2D and CD226. Furthermore, DCA may increase the expression of mitochondrial biogenesis genes and increase cell size.

Supplementary Files

This is a list of supplementary files associated with this preprint. Click to download.

- FIG3G.mp4
- SupplementalFig2.tif
- SupplementalFig3.tif
- SupplementalFig1.tif
- SupplementalFig5.tif
- SupplementalFig4.tif
- SupplementalFig6.tif